A new WENO-based momentum advection scheme for simulations of ocean mesoscale turbulence

Simone Silvestri[1], Gregory L. Wagner[1], Jean-Michel Campin[1], Navid C. Constantinou[2], Christopher N. Hill[1], Andre Souza[1], and Raffaele Ferrari[1]

[1]Massachusetts Institute of Technology, Cambridge, MA, USA
[2]Australian National University, Canberra, ACT, Australia

Key Points:

- We describe a new momentum advection scheme based on upwind-biased, weighted essentially non-oscillatory (WENO) reconstructions.
- The new scheme automatically adapts to horizontal resolution without generating grid-scale noise typical of low order oscillatory schemes.
- We demonstrate a higher "effective" resolution compared to other widely used approaches.

Abstract
Current eddy-permitting and eddy-resolving ocean models require dissipation to prevent a spurious accumulation of enstrophy at the grid scale. We introduce a new numerical scheme for momentum advection in large-scale ocean models that involves upwinding through a weighted essentially non-oscillatory (WENO) reconstruction. The new scheme provides implicit dissipation and thereby avoids the need for an additional explicit dissipation that may require calibration of unknown parameters. This approach uses the rotational, "vector invariant" formulation of the momentum advection operator that is widely employed by global general circulation models. A novel formulation of the WENO "smoothness indicators" is key for avoiding excessive numerical dissipation of kinetic energy and enstrophy at grid-resolved scales. We test the new advection scheme against a standard approach that combines explicit dissipation with a dispersive discretization of the rotational advection operator in two scenarios: *(i)* two-dimensional turbulence and *(ii)* three-dimensional baroclinic equilibration. In both cases, the solutions are stable, free from dispersive artifacts, and achieve increased "effective" resolution compared to other approaches commonly used in ocean models.

Plain Language Summary

High-resolution climate models that resolve the cyclones and anticyclones in the ocean, often called "eddies", must prevent an artificial build-up of whirl-like movements, or "enstrophy", at the model's grid-scale. But even though methods that prevent artificial accumulation of enstrophy are included only to ensure numerical stability, they unfortunately also negatively impact the quality of the model predictions even at scales larger than the grid-scale. Here, we devise a novel numerical method to overcome this deficiency. Our method has the best of both worlds: it removes just enough enstrophy so that the flow is as close to reality as possible and it achieves this without accumulating enstrophy at grid-scale.

Corresponding author: Simone Silvestri, `silvestri.simone0@gmail.com`

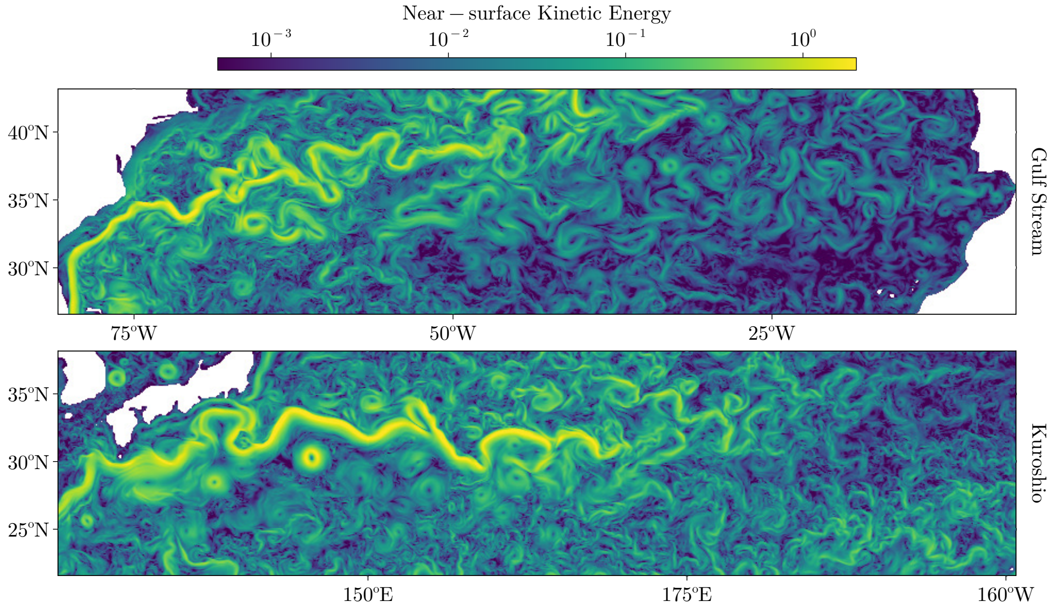

Figure 1. Near-surface kinetic energy in the Gulf stream (top panel) and the Kuroshio current (bottom panel) on March 1st from a global ocean simulation at 1/12-th of a degree horizontal resolution and 100 vertical levels that uses the novel advection scheme we introduce here as a momentum closure.

1 Introduction

Mesoscale ocean turbulence, characterized by eddies ranging from 10 to 100 kilometers in size, plays a crucial role in mixing heat, salt, momentum, and biogeochemical tracers throughout the ocean. This mixing in turns exerts a leading-order control on the large-scale ocean circulation and its impact on climate (Vallis, 2017). Until recently, climate models used ocean grids coarser than 100 km and resorted to parameterize this turbulence. The existing parameterizations (Gent & Mcwilliams, 1990) remain quite uncertain and contribute significant uncertainties to climate projections. In the last few years it has become possible to run global ocean simulations with fine grids in the 10–25 km range that partially resolve the mesoscale turbulence. This resolution is referred to as "eddy-permitting" in contrast to the "eddy-resolving" resolution that requires even finer grids, beyond presently available computational resources for climate projections (Ding et al., 2022; Silvestri et al., 2023). The eddy-permitting regime shares conceptual similarities with the well-established Large Eddy Simulation (LES) technique used in computational fluid dynamics for three-dimensional turbulence. In both cases, the grid resolution resolves only the largest turbulent eddies. The goal of this paper is to exploit this similarity and develop an accurate numerical scheme for mesoscale turbulence.

Numerical schemes for momentum advection can be categorized into two types based on the numerical characteristics of the leading order truncation term: *dispersive* and *diffusive*. Global ocean models typically rely on dispersive schemes and mitigate the dispersive "noise" by adding explicit diffusive closures (Adcroft et al., 2019; Su et al., 2018). These closures range from simple laplacian/bilaplacian diffusion with static viscosity (Schwarzkopf et al., 2019; Li et al., 2020) to more complex dynamical viscosities inspired by Large Eddy Simulations (LES) (Smagorinsky, 1963; Fox-Kemper & Menemenlis, 2004; Bachman et al., 2017). Conversely, diffusive numerical schemes exhibit a leading order diffusive error that ensures stability, eliminating the need for additional explicit closures. Examples of such schemes include flux-limited advection (Van Leer, 1977; Zalesak, 1979), piecewise-parabolic methods (Woodward

& Colella, 1984; Sytine et al., 2000), semi-Lagrangian advection (Bates & McDonald, 1982), and essentially non-oscillatory schemes (Osher & Shu, 1991).

A major advantage of diffusive numerical schemes is that they avoid a key drawback of explicit closures: the need to calibrate unknown free parameters to adapt to resolution. As importantly, they suppress spurious numerical modes caused by dispersion errors typical of centered reconstruction schemes. Explicit closures, instead, often require additional tweaking to dampen spurious computational modes as will be illustrated in idealized test cases. This reduces the effective resolution of the simulation, because the smallest scales are compromised by numerics, and may even affect the accuracy of the large-scale solutions since the mesoscale regime is characterized by a vigorous inverse energy cascade (Pressel et al., 2017).

A disadvantage of diffusive schemes is that momentum diffusion is built in the numerical reconstruction, rather than explicitly prescribed. Thus the overall dissipation cannot be easily controlled and can exceed that of explicit closures. To avoid this, the reconstruction schemes must be designed to minimize energy dissipation by utilizing stencils of sufficiently high order. Another notable drawback of implicit diffusion is that assessing energy budgets is more complicated than with energy-conserving dispersive methods stabilized by explicit dissipation. Hence, the choice of a diffusive method over a dispersive approach requires substantial evidence of significant accuracy benefits.

In this paper, we introduce a novel diffusive numerical scheme designed to reduce both the energy dissipation and the noise at the grid scale, thereby increasing the effective resolution of the model and improving numerical stability. Importantly, the new scheme holds the promise to reduce the computational cost of “eddy-resolving” ocean simulations which could be achieved with coarser grids than with presently used schemes.

Diffusive numerical schemes has seen application in various computational fluid dynamics fields, especially in combination with the conservative (or “flux-form”) formulation of the advection operator (Karaca et al., 2012; Maulik & San, 2018; Zeng et al., 2021), including in atmospheric models (Smolarkiewicz & Margolin, 1998; Souza et al., 2023; Norman et al., 2023) and regional ocean models (Shchepetkin & McWilliams, 1998a; Holland et al., 1998; Mohammadi-Aragh et al., 2015). However, finite-volume general circulation models (GCMs) often favor the rotational formulation of the advection operator due to its ease of implementation with non-regular grids, such as the cubed sphere grid (Ronchi et al., 1996), the latitude-longitude capped grid (Fenty & Wang, 2020), or the tripolar grid (Madec & Imbard, 1996). Within the rotational framework, the application of upwinding-based numerical schemes is far less common. Hahn and Iaccarino (2008) introduced upwinding in the rotational three-dimensional Navier–Stokes equations applied to the kinetic energy gradient, while Ringler (2011) described the upwinding of vorticity in the vorticity flux term as a possible monotone, diffusive discretization of the advection operator in the rotational form. The latter approach, which aligns more with the intrinsic dynamics of two-dimensional flows that are characterized by a forward enstrophy cascade, has been implemented by Roullet and Gaillard (2022) in the rotational form of the shallow-water equations using a weighted essentially non-oscillatory (WENO) reconstruction scheme.

Despite this recent progress, a mature formulation of a rotational-based upwind-biased numerical scheme for the primitive equations [1] solved by GCMs, is still lacking. Here, we take inspiration from Roullet and Gaillard (2022) and develop a WENO reconstruction scheme tailored to the rotational formulation of the advection operator, applicable to both the two-dimensional Navier–Stokes and the primitive equations. We propose this scheme as an alternative to the commonly used approach for tackling mesoscale turbulence in eddy-permitting ocean simulations, which employs explicit viscous closures paired with low-order

[1] The Navier–Stokes equations under the hydrostatic approximation are referred to as the primitive equations in the atmospheric and ocean modeling literature.

oscillatory (dispersive) advection schemes (Adcroft et al., 2019; Ding et al., 2022). Our method is constructed with two objectives in mind: *(i)* ensuring stability through variance dissipation of both rotational and divergent motions, eliminating the need for additional explicit dissipation, and *(ii)* controlling the implicit numerical diffusion through a novel approach to smoothness metrics in the WENO framework. The outcome is a method that delivers a higher "effective" resolution of the mesoscale turbulent spectra in eddy-permitting ocean simulations when compared to the approaches tested in this paper. Figure 1 shows snapshots of the surface kinetic energy from a global ocean simulation run at the "eddy permitting" lateral resolution of 1/12th degree using the novel method. The solution is characterized by a rich web of well-resolved sharp jets without grid-scale noise. We will show that traditional explicit schemes generate much noisier solutions at the grid-scale at the same resolution.

The paper is organized as follows. In section 2 we derive the new formulation of the rotational advection operator that lends itself to a diffusive discretization. In section 3, we describe the WENO reconstruction scheme and show how it can be applied to fluxed quantities in the context of the rotational form of the primitive equations. We test our newly defined WENO reconstruction in the context of two-dimensional decaying turbulence in section 4 and, finally, in section 5 we test the new rotational-based advection operator as a momentum closure alternative in an idealized baroclinic jet case. We conclude with some discussion in section 6.

2 An upwinding approach applied to the rotational form of the primitive equations

Ocean mesoscale turbulence is characterized by an inverse cascade of energy from small to large scales, weak energy dissipation, and a forward cascade of enstrophy terminated by enstrophy dissipation at small scales. Typical finite-volume discretizations of the primitive equations generate oscillatory noise at small scales that must be countered with explicit dissipation, typically via an empirical hyperviscosity. The objective of this section is to explore an alternative discretization of the primitive equations that is inherently diffusive and therefore does not generate oscillatory grid-scale noise. Specifically, we propose a discretization that effectively diffuses vorticity and horizontal divergence, enabling precise control of the dissipation of both rotational and divergent modes.

2.1 High-level description of the upwinding strategy

To provide an introductory sketch of our discretization, consider the rotational form of the advective terms in the horizontal momentum equations,

$$
\begin{aligned}
D_t u &= \overbrace{\partial_t u}^{\text{time derivative}} + \overbrace{\zeta v}^{\text{vorticity flux}} - \overbrace{w \partial_z u}^{\text{vertical advection}} - \overbrace{\partial_x K}^{\text{kinetic energy gradient}} , && (1)\\
D_t v &= \underbrace{\partial_t v}_{\text{time derivative}} - \underbrace{\zeta u}_{\text{vorticity flux}} - \underbrace{w \partial_z v}_{\text{vertical advection}} - \underbrace{\partial_y K}_{\text{kinetic energy gradient}} , && (2)
\end{aligned}
$$

where u, v are the horizontal velocity components, $\zeta \stackrel{\text{def}}{=} \partial_x v - \partial_y u$ is the vertical vorticity, and $K \stackrel{\text{def}}{=} \frac{1}{2}\left(u^2 + v^2\right)$ is the horizontal kinetic energy. Mass conservation is enforced by the continuity equation for an incompressible fluid like seawater,

$$
\underbrace{\partial_x u + \partial_y v}_{\stackrel{\text{def}}{=} d} = -\partial_z w \,, \tag{3}
$$

where we have defined the horizontal divergence, d.

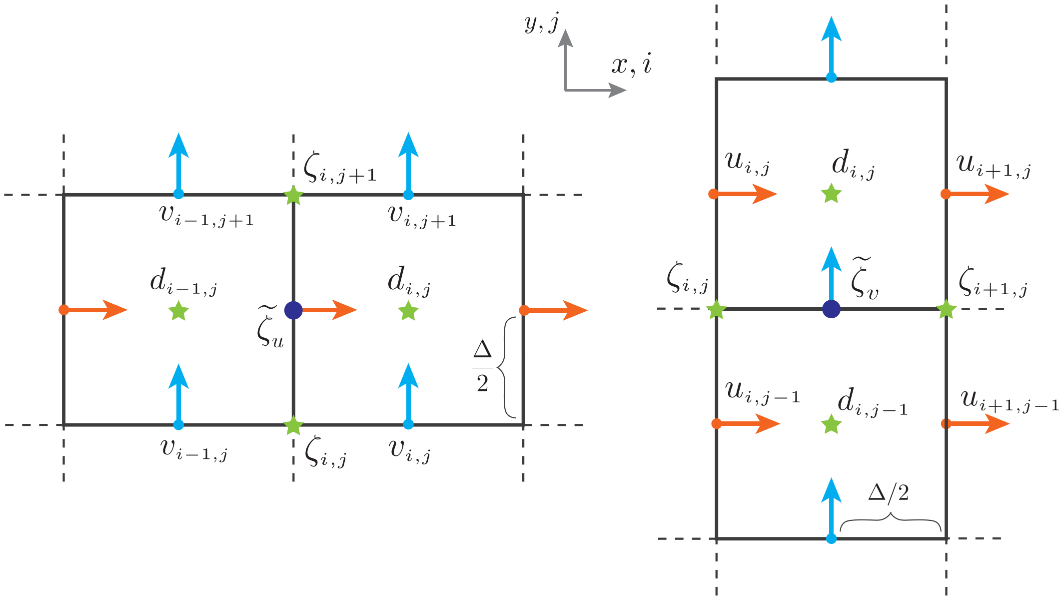

Figure 2. A sketch showing the variables' relative location on a staggered C-grid. Red and blue arrows denote the location of u- and v-velocity components, respectively; green stars show the location of vertical vorticity and horizontal divergence. Purple circles (ζ_u and ζ_v) are the *average* vorticities required to calculate the vorticity flux at u locations (left) and at v locations (right).

To lighten the notation we outline our discretization on a horizontally-isotropic rectilinear grid with regular horizontal spacing Δ. The discretization follows the staggered C-grid finite volume approach shown in Arakawa and Lamb (1977). A simplified representation of the variables' relative location on the discrete grid is shown in figure 2.

We use the vorticity flux to exemplify the numerical error associated with the widely used momentum advection schemes in computational oceanography. In a finite volume framework, it is customary to approximate the cell-averaged vorticity flux as the product of the average vorticity and the averaged velocity. An "enstrophy-conserving" (Arakawa, 1966) discretization on a C-grid requires the *reconstruction* of average vorticity at the velocity locations (see figure 2) where ζ_u and ζ_v express the *true* value of vorticity averaged in the volumes corresponding to velocity locations. Using a centered second-order approximation, denoted here with angle brackets:

$$\zeta_u \approx \langle \zeta \rangle^j \stackrel{\text{def}}{=} \frac{\zeta_{i,j+1} + \zeta_{i,j}}{2}\,, \text{ for use in } \zeta v\,, \tag{4}$$

$$\zeta_v \approx \langle \zeta \rangle^i \stackrel{\text{def}}{=} \frac{\zeta_{i+1,j} + \zeta_{i,j}}{2}\,, \text{ for use in } \zeta u\,. \tag{5}$$

We compute the numerical error $\mathcal{N}_\zeta$ by assuming that Δ is small and performing a Taylor expansion

$$\zeta_{i,j+1} = \zeta_u + \frac{\Delta}{2}\partial_y\zeta + \frac{\Delta^2}{8}\partial_y^2\zeta + \frac{\Delta^3}{48}\partial_y^3\zeta + \mathcal{O}(\Delta^4)\,, \tag{6}$$

$$\zeta_{i,j} = \zeta_u - \frac{\Delta}{2}\partial_y\zeta + \frac{\Delta^2}{8}\partial_y^2\zeta - \frac{\Delta^3}{48}\partial_y^3\zeta + \mathcal{O}(\Delta^4)\,, \tag{7}$$

where

$$\frac{\zeta_{i,j+1} + \zeta_{i,j}}{2} = \zeta_u + \mathcal{N}_\zeta\,, \qquad \text{with} \qquad \mathcal{N}_\zeta = \frac{\Delta^2}{8}\partial_y^2\zeta + \mathcal{O}(\Delta^4)\,. \tag{8}$$

In the same way, a centered discretization of the y-momentum vorticity flux leads to $\mathcal{N}_\zeta \sim \Delta^2\partial_x^2\zeta$ in (2). This truncation error is proportional to an even derivative of the vorticity field and therefore an odd derivative of the momentum field, acting as an additional spurious dispersion term in the momentum equations. By constructing $\partial_x(2) - \partial_y(1)$, we can see that the same error is dispersive also in the vorticity evolution equation and leads to additional numerical rotational modes.

The vorticity flux is not the only term that leads to dispersion, the same analysis (not done here) shows that a centered reconstruction of the vertical velocity in the vertical advection term leads to a numerical error that is proportional to the horizontal divergence

$$\mathcal{N}_d \sim \Delta^2 \int_0^z (\partial_x^2 d)\,\mathrm{d}z \;\text{ in (1)}\,, \quad \text{and} \quad \mathcal{N}_d \sim \Delta^2 \int_0^z (\partial_y^2 d)\,\mathrm{d}z \;\text{ in (2)}\,. \tag{9}$$

Here we have neglected the errors associated with the z-discretization since dispersive errors generated by the horizontal discretization are generally larger than vertical ones in typical ocean simulations where the grid cells are highly anisotropic.

We seek to improve the numerical error associated with vorticity reconstruction both by reducing its magnitude and also by computing the reconstruction so that the error is diffusive, and therefore "smooth", rather than dispersive and "noisy". For this we follow Ringler (2011), who proposed an upwind reconstruction of vorticity in the context of two-dimensional turbulence. Upwind reconstructions are diffusive: an upwind reconstruction of quantity a with respect to a velocity u leads to a truncation error that is proportional to $|u|\partial^n a$, with n an odd exponent equal to the upwinding order (Norman et al., 2023). The error of upwind vorticity reconstruction is proportional to an odd derivative of vorticity – hence an even derivative of the velocity field – and acts as a diffusion of momentum in the momentum equations:

$$\mathcal{N}_\zeta \sim \Delta^n |v| \partial_y^n \zeta \;\text{ in (1)}\,,\; \mathcal{N}_\zeta \sim \Delta^n |u| \partial_x^n \zeta \;\text{ in (2)}\,. \tag{10}$$

This error will act diffusively also in the vorticity evolution equation as it is an even derivative of the vorticity, dissipating enstrophy in accordance with the forward enstrophy cascade characteristic of a two-dimensional flow.

Next, we turn to the vertical advection term. An upwind reconstruction of vertical advection in the rotational formulation is not achieved as easily as vorticity reconstruction or flux-form reconstruction (for example, as in Shchepetkin and McWilliams (1998b)), since the major source of dispersion is the advecting variable (w) rather than the vertical reconstruction of the advected quantity ($\partial_z u$). One of the major contributions of this work is to disentangle the dispersion related to the divergence field from a conservative vertical advection, by rewriting the vertical advection term using (3) such that

$$D_t u = \overbrace{\partial_t u}^{\text{time derivative}} + \overbrace{\zeta v}^{\text{vorticity flux}} - \overbrace{u\,d}^{\text{divergence flux}} - \overbrace{\partial_z(wu)}^{\text{conservative vertical advection}} - \overbrace{\partial_x K}^{\text{kinetic energy gradient}}\,, \tag{11}$$

$$D_t v = \underbrace{\partial_t v}_{\text{time derivative}} - \underbrace{\zeta u}_{\text{vorticity flux}} - \underbrace{v\,d}_{\text{divergence flux}} - \underbrace{\partial_z(wv)}_{\text{conservative vertical advection}} - \underbrace{\partial_y K}_{\text{kinetic energy gradient}}\,. \tag{12}$$

We have thus relegated the horizontal dispersive error, tied to the vertical velocity w, to a "divergence flux" term, akin to the vorticity flux. Contrary to the vertical advection terms in (1)–(2), the "divergence fluxes" in (11)–(12) are clearly amenable to an upwinding strategy. In particular, we use an upwind reconstruction of d with respect to u in ud term in (11), and vice versa an upwind reconstruction of d with respect to v in vd term in (12), which changes the dispersive error in (9) to

$$\mathcal{N}_d \sim \Delta^n |u| \partial_x^n d \;\text{ in (1)}\,, \quad \text{and} \quad \mathcal{N}_d \sim \Delta^n |v| \partial_y^n d \;\text{ in (2)}\,. \tag{13}$$

Deriving the horizontal divergence evolution equation $\partial_x(1) + \partial_y(2)$ shows that this approach leads to a direct diffusion of the horizontal divergence. This implementation allows a mitigation of the dispersion inherent in the vertical velocity field as it removes spurious numerical divergent modes similar to how vorticity upwinding removes spurious numerical rotational modes.

2.2 Detailed implementation in the discrete primitive equations

We concretize the approach explained above on an orthogonal C-grid, where we define cell volumes $\mathscr{V}_u$, $\mathscr{V}_v$, $\mathscr{V}_w$, and $\mathscr{V}_c$ for volumes at the $u-$, $v-$, $w-$velocity and tracer locations, respectively. The facial areas are denoted with $\mathscr{A}_x$, $\mathscr{A}_y$, and $\mathscr{A}_z$ and the spacings with Δx, Δy and Δz. As for volumes, we will use subscripts u, v, and w to denote the location of spacings Δx, Δy, and Δz. In addition to the angle bracket notations, we use double brackets and δ to express double-centered reconstructions and finite differences, respectively:

$$\langle\!\langle a \rangle\!\rangle^{ij} \stackrel{\text{def}}{=} \left\langle \langle a \rangle^i \right\rangle^j \ , \quad \text{and} \quad \delta_i a \stackrel{\text{def}}{=} a_{i+1} - a_i \, . \tag{14}$$

Additionally, we use curly braces $\{\cdot\}$ to indicate upwinding where $\{a\}^i$ denotes an upwind reconstruction of variable a in the x-direction with respect to the x-velocity component (u). The specific formulation of the upwind reconstruction we use in this paper will be shown in section 3.

We indicate the discrete counterpart to the vorticity flux, the vertical advection, and the kinetic energy gradient, with $\mathcal{Z}$, $\mathcal{V}$, and $\mathcal{K}$, respectively. We use subscripts u and v to denote the x-momentum and y-momentum components of the discrete terms. As the material derivative of momentum (1)-(2) is discretized as follows:

$$D_t u = \partial_t u + \mathcal{Z}_u - \mathcal{V}_u - \mathcal{K}_u \, , \tag{15}$$

$$D_t v = \partial_t v - \mathcal{Z}_v - \mathcal{V}_v - \mathcal{K}_v \, , \tag{16}$$

We review here the centered-second order discretization schemes typically used in ocean modeling. The "energy conserving" centered second-order discretization of the vorticity flux term (Arakawa, 1966), later used as a reference, is

$$\mathcal{Z}_u^E = \frac{\left\langle \langle \Delta x_v v \rangle^i \zeta \right\rangle^j}{\Delta x_u} \, , \quad \mathcal{Z}_v^E = \frac{\left\langle \langle \Delta y_u u \rangle^j \zeta \right\rangle^i}{\Delta y_v} \, . \tag{17}$$

The "enstrophy conserving" centered second-order discretization of the vorticity flux term (Arakawa, 1966) in this notation is

$$\mathcal{Z}_u = \frac{\langle\!\langle \Delta x_v v \rangle\!\rangle^{ij}}{\Delta x_u} \langle \zeta \rangle^j \ , \ \mathcal{Z}_v = \frac{\langle\!\langle \Delta y_u u \rangle\!\rangle^{ij}}{\Delta y_v} \langle \zeta \rangle^i \, . \tag{18}$$

$\mathcal{K}$ is usually formulated as (Madec et al., 2022)

$$\mathcal{K}_u = \frac{\left\langle \delta_i u^2 \right\rangle^i + \left\langle \delta_i v^2 \right\rangle^j}{2\Delta x_u} \, , \ \mathcal{K}_v = \frac{\left\langle \delta_j u^2 \right\rangle^i + \left\langle \delta_j v^2 \right\rangle^j}{2\Delta y_v} \, , \tag{19}$$

while the discrete vertical advection $\mathcal{V}$ is derived from $\mathcal{K}$ to ensure the following integral energy conservation property (Madec et al., 2022):

$$\sum_{i,j,k} (u\mathscr{V}_u \mathcal{V}_u + v\mathscr{V}_v \mathcal{V}_v) + \sum_{i,j,k} (u\mathscr{V}_u \mathcal{K}_u + v\mathscr{V}_v \mathcal{K}_v) = 0 \, . \tag{20}$$

This property ensures that the change in discrete energy from the vertical advection term is balanced by the kinetic energy gradient. When paired with an energy-conserving vorticity flux implementation, the overall scheme conserves discrete energy in the system. The resulting formulation for $\mathcal{V}$ is:

$$\mathcal{V}_u = \frac{\left\langle \langle W \rangle^i \delta_k u \right\rangle^k}{\mathscr{V}_u} \, , \quad \mathcal{V}_v = \frac{\left\langle \langle W \rangle^j \delta_k v \right\rangle^k}{\mathscr{V}_v} \, . \tag{21}$$

The first step is to derive a suitable discrete form for the conservative vertical advection - divergence flux form of the material derivatives (11)-(12). We denote with $\mathcal{C}$ and $\mathcal{D}$ the discrete counterpart to the conservative vertical advection and the divergence flux. To derive suitable candidates for $\mathcal{C}$ and $\mathcal{D}$, we manipulate $\mathcal{V}$ to ensure discrete energy conservation through

$$\sum_{i,j,k} (u\mathscr{V}_u\mathcal{V}_u + v\mathscr{V}_v\mathcal{V}_v) = \sum_{i,j,k} \Big[u\mathscr{V}_u(\mathcal{C}_u + \mathcal{D}_u) + v\mathscr{V}_v(\mathcal{C}_v + \mathcal{D}_v)\Big] . \tag{22}$$

The derivation is performed in Appendix B (note that $\mathcal{V} \neq \mathcal{C} + \mathcal{D}$ locally). The resulting discrete formulations read

$$\mathcal{C}_u = \frac{\delta_k \left(\langle W\rangle^i \langle u\rangle^k\right)}{\mathscr{V}_u} , \mathcal{C}_v = \frac{\delta_k \left(\langle W\rangle^j \langle v\rangle^k\right)}{\mathscr{V}_v} , \tag{23}$$

$$\mathcal{D}_u = \frac{u\,\langle D\rangle^i}{\mathscr{V}_u} , \qquad \mathcal{D}_v = \frac{v\,\langle D\rangle^j}{\mathscr{V}_v} , \tag{24}$$

where $D = \delta_i U + \delta_j V$ is the discrete horizontal divergence, $U = \mathscr{A}_x u$, $V = \mathscr{A}_y v$, and $W = \mathscr{A}_z w$. With a formulation for $\mathcal{C}$ and $\mathcal{D}$, we have found a suitable, energy-conserving discretization of equations (11)-(12):

$$D_t u = \partial_t u + \mathcal{Z}_u - \mathcal{D}_u - \mathcal{C}_u - \mathcal{K}_u , \tag{25}$$

$$D_t v = \partial_t v - \mathcal{Z}_v - \mathcal{D}_v - \mathcal{C}_v - \mathcal{K}_v . \tag{26}$$

The second step consists in correctly upwinding fluxed variables. Following our approach, we implement an upwind reconstruction of vorticity in (18) by substituting the following terms

$$\langle\zeta\rangle^i \mapsto \{\zeta\}^i \text{ and } \langle\zeta\rangle^j \mapsto \{\zeta\}^j . \tag{27}$$

The same can be done for $\mathcal{C}$ and $\mathcal{D}$, where an upwind reconstruction is ensured by

$$\langle u\rangle^k \mapsto \{u\}^k \text{ and } \langle v\rangle^k \mapsto \{v\}^k , \tag{28}$$

$$\langle D\rangle^i \mapsto \{D\}^i \text{ and } \langle D\rangle^j \mapsto \{D\}^j . \tag{29}$$

As we show in Appendix C, numerical errors that scale with a cross-derivative of the velocity field can lead to grid-scale energy generation instead of energy dissipation. For example, since $d = \partial_x u + \partial_y v$, a straightforward first-order upwind reconstruction of d in the x-direction leads to

$$\mathcal{N}_d \sim |u|(\partial_x^2 u + \partial_x\partial_y v) , \tag{30}$$

where $\partial_x^2 u$ is diffusive while $\partial_x\partial_y v$ has the potential to be anti-diffusive. The opposite happens in the y-direction. To avoid injecting energy at the grid scale, we define the upwind reconstruction of the discrete divergence as a reconstruction that guarantees discrete energy dissipation. For this reason, we implement upwinding of D as follows

$$\{D\}^i \overset{\text{def}}{=} \{\delta_i U\}^i + \langle\delta_j V\rangle^i , \tag{31}$$

$$\{D\}^j \overset{\text{def}}{=} \langle\delta_i U\rangle^j + \{\delta_j V\}^j . \tag{32}$$

We follow the same implementation for $\mathcal{K}$, where we recognize the similarity between $\mathcal{D}$ and $\mathcal{K}$ ($u\partial_x u = \frac{1}{2}\partial_x u^2$ and $v\partial_y v = \frac{1}{2}\partial_y v^2$) and can safely substitute

$$\left\langle\delta_i u^2\right\rangle^i \mapsto \left\{\delta_i u^2\right\}^i \text{ and } \left\langle\delta_j v^2\right\rangle^j \mapsto \left\{\delta_j v^2\right\}^j , \tag{33}$$

in equation (19).

The approach we sketched results in a method that is energetically dissipative, tackles stability issues through an upwinding strategy, and removes grid-scale variance when applied to the rotational form of the primitive equations. The main ingredients are the splitting of the vertical advection term (11)-(12), the discrete energy conserving implementation (23)-(24)

followed by the targeted upwind substitutions (27), (28), (29), and (33). We have not yet described how to perform the upwinding, which, in principle, can be done with any diffusive reconstruction scheme. In the next section, we propose a WENO-based reconstruction that pairs with the discretization detailed above by allowing a notably lower level of energy dissipation compared to other upwinding strategies.

3 WENO reconstruction scheme for the rotational primitive equations

The Weighted Essentially Non-Oscillatory (WENO) scheme is a particular implementation of the Essentially Non-Oscillatory schemes first introduced by Harten et al. (1987) and refined by Shu (1997). The WENO scheme is especially appropriate to resolve shocks that develop in solutions of partial differential equations such as the Euler equations or the shallow water equations. The central idea behind the WENO scheme is to dynamically approximate a numerical flux with multiple low-order reconstructing polynomials. These polynomials are combined using nonlinear weights that depend on the smoothness of each individual polynomial, with the objective of obtaining a high-order upwind reconstruction in smooth regions and lower-order upwind reconstruction in regions where the solution is less smooth. This approach allows the scheme to achieve high accuracy even in regions of high gradients and discontinuities while, at the same time, avoiding artificial oscillations (dispersive artifacts) that plague conventional high-order methods.

We start by reviewing the mathematical implementation of a WENO reconstruction. Given a discrete quantity ϕ, we denote with $[\phi]^i_r$ the one-dimensional reconstruction obtained by the r-th candidate polynomial of order s ($p_{r\phi}$ for $r \in \{0, \dots, s-1\}$) in the i-th direction, that is:

$$[\phi]^i_r \stackrel{\text{def}}{=} p_{r\phi}(x_{i+1/2}) = \sum_{j=0}^{s-1} c_{rj}\phi_{i-r+j} \ , \ \text{with} \ \ r \in \{0, \dots, s-1\} \, . \tag{34}$$

where ϕ_{i-r+j} is the average ϕ in cell $i-r+j$, c_{rj} are linear reconstructing weights and $x_{i+1/2}$ is the final x position of $[\phi]^i_r$ on the discrete grid (Shu, 1997). The WENO reconstruction procedure is a convex combination of the candidate reconstructions and is implemented as follows:

$$\{\phi\}^i = \sum_{r=0}^{s-1} \xi_{r\phi}[\phi]^i_r \ , \ \text{with} \ \xi_{r\phi} = \frac{\alpha_{r\phi}}{\sum_{r=0}^{s-1}\alpha_{r\phi}} \ \text{and} \ \alpha_{r\phi} = f(\alpha^\star_r, \beta_{r\phi}) \, . \tag{35}$$

Above, ξ_r are the nonlinear WENO weights, which are functions of the optimal linear weights ($\alpha^\star_r$) weighted by a measure of smoothness of the field $\beta_{r\phi}$, where the subscript ϕ indicates that β is calculated from field ϕ. The $\alpha^\star_r$ optimal linear weights are obtained by equating the final reconstruction $\{\phi\}^i$ to a classical upwind biased reconstruction of order $2s-1$ when the field ϕ is smooth ($\beta_{r\phi} = 0$ for each $r \in \{0, \dots, s-1\}$). Several formulations for smoothness weighting (f) have been put forth, and, while the exact formulation of the α weights is not a central concern of this work, it is noteworthy to mention that we employ the WENO-Z formulation (Balsara & Shu, 2000). In terms of smoothness indicators, the most widespread approach is to use a Sobolev norm of the reconstructing polynomial $p_{r\phi}$ over the interval $(x_{i-1/2}, x_{i+1/2})$ (Shu, 1997):

$$\beta_{r\phi} \stackrel{\text{def}}{=} \sum_{\ell=1}^{s-1} \int_{x_{i-1/2}}^{x_{i+1/2}} \Delta x^{2\ell-1} \left(\partial^\ell_x p_{r\phi}\right)^2 \mathrm{d}x \ . \tag{36}$$

The Sobolov norm is larger for polynomials characterized by larger gradients, thus connecting the "smoothness" of a polynomial to the size of its derivatives of order 1 to $s-1$ (in the range $x_{i-1/2}$ to $x_{i+1/2}$).

For "flux-form" advection, the reconstructed field is typically the same as the field that is advanced in time. As such, using ϕ to compute β_r, directly connects the smoothness evaluation to the evolved quantity. This is not the case in the rotational form of the Navier–Stokes equations where the field evolved in time is typically not the same as the field being reconstructed. Specifically, in the derivation outlined in the preceding section, upwind reconstruction is applied to six distinct quantities:

$$\{\zeta\}^j\,,\ \{u\}^k\,,\ \{D\}^i\,,\ \left\{\delta_i u^2\right\}^i \quad \text{in the } u \text{ evolution equation,} \tag{37}$$

$$\{\zeta\}^i\,,\ \{v\}^k\,,\ \{D\}^j\,,\ \left\{\delta_j v^2\right\}^j \quad \text{in the } v \text{ evolution equation.} \tag{38}$$

Many terms in (37)-(38) above involve derivatives of the velocities and thus exhibit rapid variations at the grid scale compared to the dynamics of the horizontal momentum fields. In this context, we found that $\beta_{r\phi}$ is an inadequate smoothness measure since it lacks an intuitive connection with the dynamics of the evolved field – specifically, the velocity field, which is significantly smoother than the upwinded quantities. Due to this discrepancy, $\beta_{r\phi}$ in (35) causes an artificial decrease of the WENO reconstruction order leading to a larger-than-necessary dissipation. We demonstrate this in section 4 within the context of two-dimensional decaying turbulence and in section 5 within the context of a three-dimensional baroclinic jet.

Based on the above discussion, we propose here an alternative approach to assess smoothness, wherein we employ the reconstructing polynomials of a "parent" (smoother) field constructed directly from velocities, rather than from their derivatives. An exception is the divergence flux: we find that the divergence flux term contributes the most to grid-scale noise and, as such, we choose to diffuse it consistently with its intrinsic smoothness. We introduce notation to facilitate the description and understanding of our approach. In this notation, a WENO reconstruction is denoted as

$$\{\phi;\psi\}\ , \tag{39}$$

where ϕ represents the field being reconstructed and ψ is the field used for assessing the smoothness. We use the notation $\{\phi;\psi\}^i$ as short-hand for the following reconstruction

$$\{\phi;\psi\}^i = \sum_{r=0}^{s-1} \xi_{r\psi} [\phi]_r^i\ , \tag{40}$$

where $\xi_{r\psi}$ is calculated using (35)-(36) and $p_{r\psi}$ (the reconstructing polynomials of quantity ψ). Under the conventional WENO scheme, where the reconstructed and smoothness-diagnosed fields are identical, this notation simplifies to $\{\phi;\phi\}$. Where not explicitly stated, $\{\phi\}$ denotes a WENO reconstruction with standard smoothness stencils, that is $\{\phi\} = \{\phi;\phi\}$.

The smoothness-optimized upwind WENO reconstructions, written in the above-presented notation, are

$$\{\zeta;\boldsymbol{u}\}^j\,,\ \{u\}^k\,,\ \{D;D\}^i\,,\ \left\{\delta_i u^2;\langle u\rangle^i\right\}^i \quad \text{in the } u \text{ evolution equation,} \tag{41}$$

$$\{\zeta;\boldsymbol{u}\}^i\,,\ \{v\}^k\,,\ \{D;D\}^j\,,\ \left\{\delta_j v^2;\langle v\rangle^j\right\}^j \quad \text{in the } v \text{ evolution equation,} \tag{42}$$

where we define the upwinding of ζ as an average between a u-based and a v-based reconstruction:

$$\{\zeta;\boldsymbol{u}\} \stackrel{\text{def}}{=} \frac{\left\{\zeta;\langle u\rangle^j\right\} + \left\{\zeta;\langle v\rangle^i\right\}}{2}\ . \tag{43}$$

Using reconstructed variables $\langle v\rangle$ and $\langle u\rangle$ as smoothness metrics and not u and v directly is a consequence of the staggered C-grid discretization. Note the difference between $\{D\}$ and $\{D;D\}$: while the first uses the individual velocity derivatives as a smoothness measure, the second uses the whole discrete divergence:

$$\{D\}^i = \{\delta_i U;\delta_i U\}^i + \langle\delta_j V\rangle^i\ , \quad \{D\}^j = \langle\delta_i U\rangle^j + \{\delta_j V;\delta_j V\}^j\ , \tag{44}$$

$$\{D;D\}^i = \{\delta_i U;D\}^i + \langle\delta_j V\rangle^i\ , \quad \{D;D\}^j = \langle\delta_i U\rangle^j + \{\delta_j V;D\}^j\ . \tag{45}$$

This difference has a large impact on the solution as, usually, $\delta_j V$ and $\delta_i U$ have a cancellation effect.

Table 1. Description of test cases

Name	Legend	Vorticity Flux	Vorticity smoothness	SGS closure
DNS		Energy conserving	—	—
Leith1		Energy conserving	—	Leith, $\mathbb{C}=1$
Leith2		Energy conserving	—	Leith, $\mathbb{C}=2$
W5D		WENO 5th order	$\{\zeta\}$	—
W9D		WENO 9th order	$\{\zeta\}$	—
W5V		WENO 5th order	$\{\zeta;\boldsymbol{u}\}$	—
W9V		WENO 9th order	$\{\zeta;\boldsymbol{u}\}$	—

4 Two-dimensional homogeneous decaying turbulence test case

We begin by evaluating our novel momentum advection scheme using simulations of decaying two-dimensional homogeneous turbulence. The purpose of this test is to compare our momentum advection scheme with dispersive numerics in a setting where it is computationally feasible to run Direct Numerical Simulations (DNS), i.e. simulations that resolve scales down to the physical dissipation. The DNS serves as the benchmark, allowing us to assess the performance of the different approaches at coarser resolutions. To further investigate the impact of decoupling the reconstruction polynomials from the smoothness assessment, we examine the reconstruction of vorticity using both $\{\zeta;\boldsymbol{u}\}$ and $\{\zeta\}$. This test case is well-suited to assess the discrete properties of the vorticity flux reconstruction, because there are no divergent motions in two dimensions.

We solve the incompressible two-dimensional Navier–Stokes equations in non-dimensional form, i.e.,

$$\partial_t \boldsymbol{u} + \zeta \hat{\boldsymbol{k}} \times \boldsymbol{u} = -\boldsymbol{\nabla}(p+K) + \frac{1}{Re}\nabla^2 \boldsymbol{u} + \boldsymbol{\nabla}\cdot\boldsymbol{\tau}_{\mathrm{SGS}}, \tag{46}$$

$$\boldsymbol{\nabla}\cdot\boldsymbol{u} = 0 \; . \tag{47}$$

Notice that $\boldsymbol{u}$ and $\boldsymbol{\nabla}$ denote the two-dimensional rather than the three-dimensional velocity vector and gradient in this section. The simulations are run with a $Re = 3.3\times 10^4$ on a doubly periodic box of nondimensional size $2\pi \times 2\pi$. The equations are evolved using a low-storage third-order Runge-Kutta scheme and a pressure projection method that utilizes an FFT elliptical solver.

We initialize the simulations with velocities generated through a narrow-band energy spectrum as proposed by Ishiko et al. (2009),

$$E(k) = \frac{1}{2} a_s k_p^{-1} \left(\frac{k}{k_p}\right)^7 \exp\left[-\frac{7}{2}\left(\frac{k}{k_p}\right)^2\right] , \tag{48}$$

where $k \overset{\mathrm{def}}{=} (k_x^2 + k_y^2)^{1/2}$ is the magnitude of the wavenumber vector, $a_s = 16/3$, and $k_p = 12$ is the wavenumber corresponding to maximum energy. With this choice of initial condition and Reynolds number, we achieve a good spectral separation between the energy-containing and dissipation scales. To construct a velocity field with this energy spectrum, we first generate a vorticity field in Fourier space

$$\widehat{\zeta}(k_x, k_y) = \left[\frac{k}{\pi} E(k)\right]^{1/2} e^{\mathrm{i}\phi(k_x,k_y)} \; , \tag{49}$$

where $\phi(k_x, k_y)$ are random phases chosen such that that the vorticity field in physical space is real (Ishiko et al., 2009). The initial velocity distributions are then given by:

$$\widehat{u}(k_x, k_y) = \frac{\mathrm{i}k_y}{k^2}\widehat{\zeta}(k_x, k_y) \; , \quad \widehat{v}(k_x, k_y) = -\frac{\mathrm{i}k_x}{k^2}\widehat{\zeta}(k_x, k_y) \; . \tag{50}$$

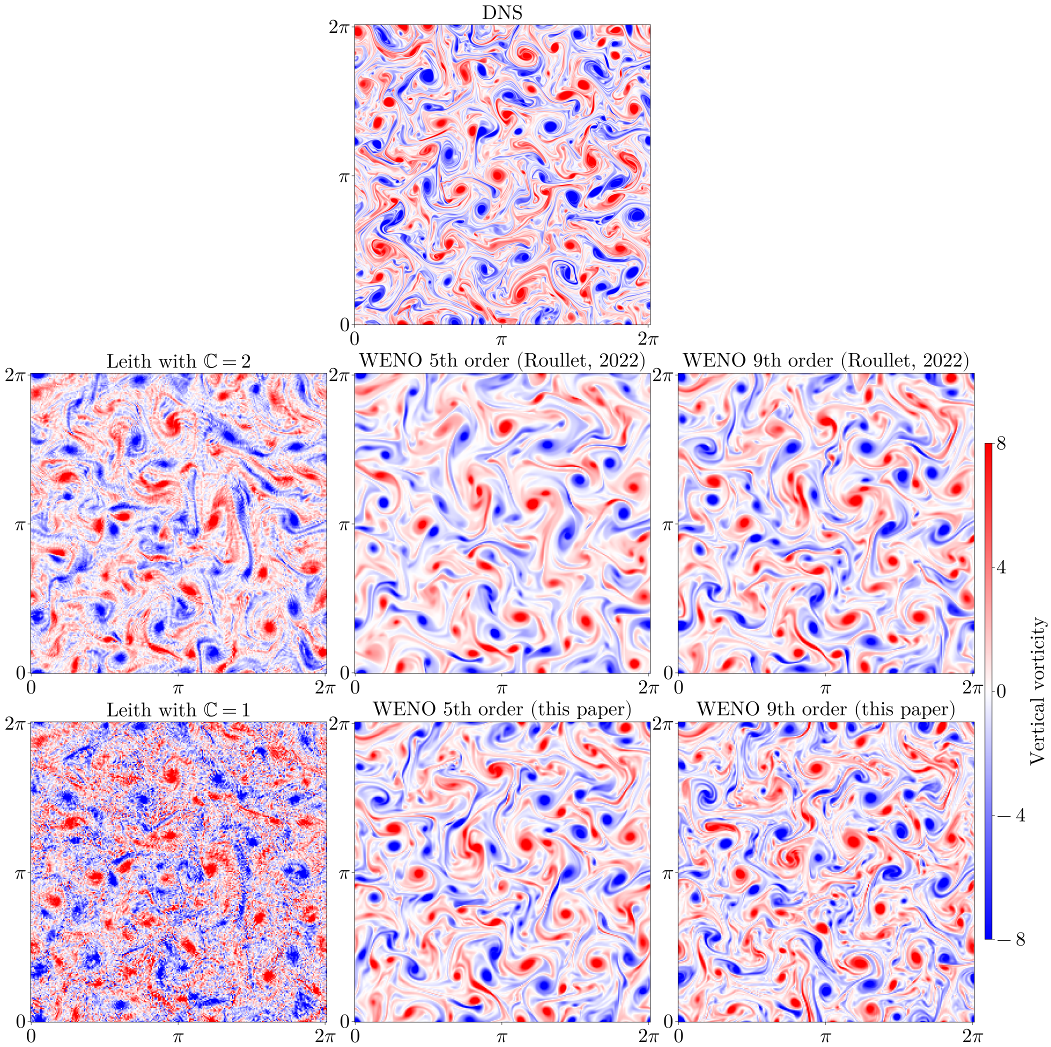

Figure 3. Vorticity at $t = 3.6$ after initialization. Comparison between DNS (top panel), explicit LES with a Leith viscosity (left panels), and implicit LES with a rotational WENO discretization with $N = 256^2$. Of the WENO schemes, the top panels show the results obtained with a standard WENO reconstruction of vorticity $\{\zeta;\zeta\}$ (W5D and W9D in table 1) while the bottom panels show a reconstruction using the velocity field as smoothness measure $\{\zeta;\boldsymbol{u}\}$ (W5V and W9V in table 1).

The simulations are run for $t = 6$ nondimensional time units. Given that the initial eddy turnover time, defined as

$$T_e = \left(\int_0^\infty k^2 E(k) dk\right)^{0.5} , \tag{51}$$

is roughly 0.33 non-dimensional time units, a time of $t = 6$ would correspond to about 18 eddy turnovers.

The fully resolved benchmark solution employs the second-order energy-conserving advection discretization, as per eq. (17) and $N = 4096 \times 4096$ grid points. We compare it with solutions obtained using coarser grids and three distinct methods. The first is a second-order energy-conserving advection operator stabilized by the Leith closure (see Appendix A). We do not consider the adaptive Leith scheme, because it is too expensive for oceanographic applications. Instead, we consider the traditional Leith scheme for two different values of the nondimensional parameter $\mathbb{C}$: $\mathbb{C} = 1$ and $\mathbb{C} = 2$. The second method involves the rotational WENO, using standard smoothness diagnosis $\{\zeta\}$ as in the work by Roullet and

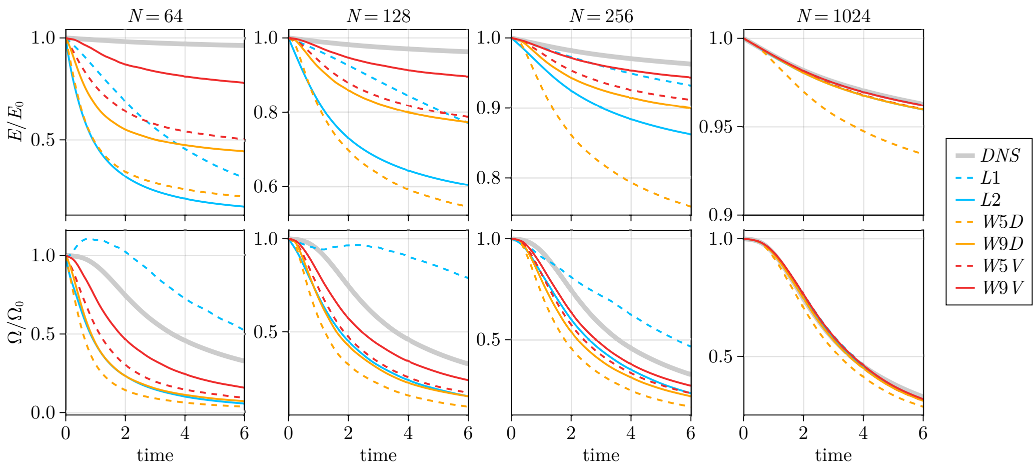

Figure 4. Evolution in time of integrated kinetic energy (top row) and integrated enstrophy (bottom row). Advection schemes and numerical details are shown in table 1.

Gaillard (2022). The third method employs the new rotational WENO, where vorticity is reconstructed as $\{\zeta; \boldsymbol{u}\}$. For the WENO schemes, we compare fifth- and ninth-order reconstruction. All the different methods are summarized in table 1.

The grid size for the under-resolved simulations is ramped up from 64×64, where only the largest structures are resolved, to 128×128, 256×256, and finally 1024×1024, where the grid is fine enough to resolve most of the energy and enstrophy spectra. For reference, in a high-resolution global ocean simulation, the grid barely resolves the largest-scale eddies and is therefore more similar to the 64×64 or 128×128 case than the 1024×1024.

Figure 3 shows a comparison of the vertical vorticity at $t = 3.6$, which corresponds to 11 turnovers referenced to the initial eddy turnover time. The top panel shows the DNS solution, while the center and bottom panels show the under-resolved simulations. The Leith closure, even when using the larger parameter $\mathbb{C} = 2$, results in substantial nonphysical noise at the grid scale. In contrast, all WENO-based reconstructions yield a turbulent solution completely devoid of grid-scale noise. The dynamics at small scales is better resolved with higher WENO order as evidenced by the appearance of well resolved structures close to the grid-scale. The same result can be noticed when switching from standard WENO smoothness stencils to $\{\zeta; \boldsymbol{u}\}$.

Figure 4 illustrates the evolution of kinetic energy (top panels) and enstrophy (bottom panels) for the various methods at different resolutions. The evolution of both quantities converges to the DNS solution at 1024×1024 for all methods as the resolution is increased, except for the WENO fifth-order with standard vorticity reconstruction (W5D) which exhibits excessive energy dissipation. As for the Leith closures, they do converge to the DNS solution at the highest resolution (1024×1024) but are severely deficient at coarser resolutions. With $\mathbb{C} = 1$, the solutions have too large enstrophy as the closure fails to remove grid-scale vorticity stemming from the centered advection scheme. With $\mathbb{C} = 2$ the enstrophy levels are reduced, but at the cost of too low kinetic energy. The difference between $\mathbb{C} = 1$ and $\mathbb{C} = 2$ illustrates the fundamental challenge with using dispersive numerical methods: removing spurious dispersive artifacts can require excessively high dissipation with the unintended consequence of reducing the large scale energy in the system. Conversely, the WENO reconstruction schemes are designed to limit dispersive artifacts while maintaining high-order reconstruction that retains large-scale energy. Figure 4 shows that, as expected, the accuracy of the WENO approach increases with a higher discretization order. Most importantly the smoothness measure obtained with the new stencils $\{\zeta; \boldsymbol{u}\}$ achieves a higher effective resolution, i.e. converges faster to the DNS solution.

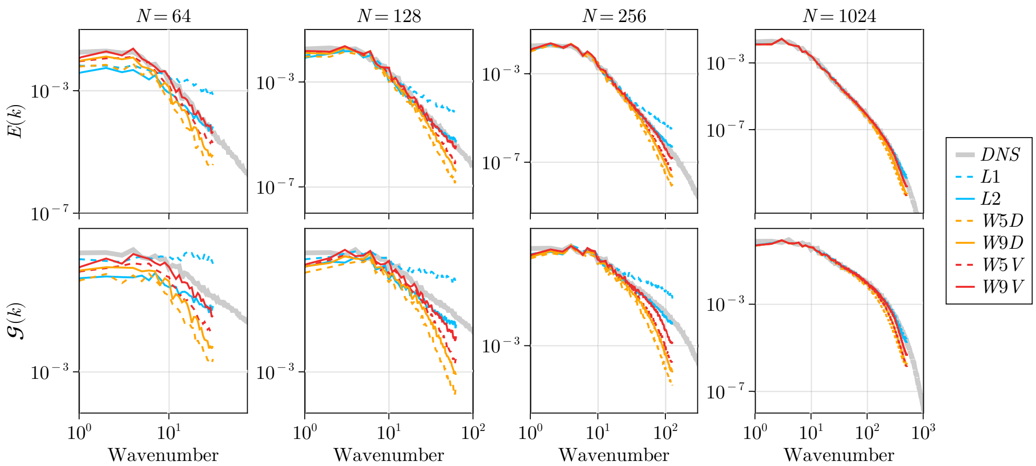

Figure 5. Kinetic energy spectra (top panels) and enstrophy spectra (bottom panels) at $t = 3.6$. Advection schemes and numerical details are shown in table 1.

Figure 5 shows the energy (top panels) and enstrophy (bottom panels) spectra at $t = 3.6$. Again, all methods converge to the DNS solution at 1024×1024 (in the inertial range), except for the W5D case. At lower resolutions, the Leith closure with $\mathbb{C} = 1$ fails to match the DNS spectra and exhibits a pile-up of variance at small scales. Using a larger parameter ($\mathbb{C} = 2$) reduces the bias in small-scale variance at the expense of excessive damping of energy, especially at large scales; this is hard to appreciate in Fig. 5 because of the logarithmic scale, but is clear in Fig. 4. WENO reconstructions do overly dissipate enstrophy at small scales, as they are designed to do, but the energy spectra are much better captured especially with the $\{\zeta; \boldsymbol{u}\}$ reconstruction. This is vindication that the upwinding of vorticity dissipates enstrophy, but not energy, at small scales. In this case, a ninth-order WENO reconstruction of vorticity, using $\{\zeta; \boldsymbol{u}\}$ stencils (W9V), captures the DNS energy spectrum at all resolutions, down to 64×64.

In conclusion, in the context of two-dimensional decaying turbulence, the explicit Leith closure accurately represents the DNS solution only at the highest resolution but fails at lower resolutions. This failure stems from the oscillatory dynamics of the centered advection scheme that produce grid-scale noise which is not selectively damped by the Leith closure. In practice, the closure results in either too much enstrophy at small scales or too little energy at all scales depending on parameter choices. In contrast, a WENO reconstruction of vorticity using $\{\zeta; \boldsymbol{u}\}$ dissipates enstrophy at small scales and preserves an accurate energy spectrum at all scales. Additionally, this test case demonstrates the benefit of using high-order reconstruction stencils, as the ninth-order scheme produces a much more energetic solution that converges to DNS at coarser resolution compared to the fifth-order counterpart. We conclude that, for this case, the W9V approach comes closer to achieving the LES goal of resolution independence than the other methods explored in this section.

5 Baroclinic jet test case

Next, we test our rotational WENO reconstruction in a baroclinic jet setup. The setup consists of a periodic channel in a spherical sector between 60°S - 40°S, 20 degrees wide, and one kilometer deep. The simulations are initialized with a constant vertical stratification

Table 2. Details of the different advection schemes used.

Method Name	Dispersive	Upwind	WENO
Rotational form $\mathcal{Z}$	Energy conserving (17)	—	WENO 9th-order
Rotational form $\mathcal{V}$	Centered 2nd-order (21)	—	—
Rotational form $\mathcal{D}$	—	—	WENO 9th-order
Rotational form $\mathcal{C}$	—	—	WENO 5th-order
Rotational form $\mathcal{K}$	Centered 2nd order (19)	—	WENO 5th-order
Flux-form advection	—	Upwind 3rd-order	—
Tracer advection	WENO 7th-order	WENO 7th-order	WENO 7th-order

Table 3. Computational details of the test cases. The advection column refers to the details shown in table 2. Each case consists of three simulations with a horizontal resolution of 1/8th, 16th, and 1/32nd of a degree.

	Advection	Smoothness	explicit closure
UP3	Upwind	—	—
W9V	WENO	Eqs. (41) and (42)	—
W9D	WENO	Eqs. (37) and (38)	—
SM2	Dispersive	—	Smagorinsky (Appendix A)
QG2	Dispersive	—	QG Leith with $\mathbb{C} = 2$ (Appendix A)

$N^2 = 4 \times 10^{-6}$ s^{-2} and a meridional buoyancy front given by:

$$b(\phi, z) = N^2 z + \Delta b \begin{cases} 0 & \text{if } \gamma(\phi) < 0 \ , \\ [\gamma(\phi) - \sin\gamma(\phi)\cos\gamma(\phi)]/\pi & \text{if } 0 \le \gamma(\phi) \le \pi \ , \\ 1 & \text{if } \pi < \gamma(\phi) \ , \end{cases} \tag{52}$$

$$\gamma(\phi) = \frac{\pi}{2} - 2\pi \frac{\phi - \phi_0}{\Delta\phi} \ , \tag{53}$$

where $\phi_0 = 50°$S is the central latitude of the domain, $\Delta\phi = 20°$ the domain's latitudinal extent, $\Delta b = 5 \times 10^{-3}$ m s^{-2}. The initial velocity is in thermal-wind balance with the buoyancy field and vanishes at $z = -H$. Thus the initial conditions are an equilibrium solution to the primitive equations, but one that is unstable to the development of baroclinic instability (Vallis, 2017).

The initial buoyancy and velocity profiles are shown in figure 6. We add a weak white noise to the profile to kick-start the baroclinic instability (not shown in the figure). We impose no-flux and free-slip boundary conditions on all solid walls. We also prescribe a background vertical viscosity $\nu = 10^{-4}$ m^2 s^{-1} and a vertical diffusivity $\kappa = 10^{-5}$ m^2 s^{-1}. To sustain turbulence and allow an equilibrated solution, we linearly restore the zonally averaged buoyancy and velocity to the initial profiles with a timescale of 50 days (in a similar manner as done by Soufflet et al. (2016)). This restoring sets the zonal transport without interfering with the development of mesoscale eddies, which are the focus of this test. We run the simulations for a total of 1000 days.

We conduct a series of simulations using different momentum advection approaches. Three dispersive schemes: (1) our novel advection scheme (W9V) with ninth-order WENO reconstruction of vorticity ($\mathcal{Z}$) and divergence ($\mathcal{D}$), and a 5th order for $\mathcal{C}$, and $\mathcal{K}$ as their order has minimal impact on the solution; (2) a WENO reconstruction of the same order with standard smoothness stencils (W9D) for both vorticity flux $\{\zeta\}$, divergence flux $\{D\}$, and kinetic energy gradient $\{\boldsymbol{\delta} \cdot \boldsymbol{u}^2\}$; (3) a third-order flux-form upwind-biased advection (UP3),

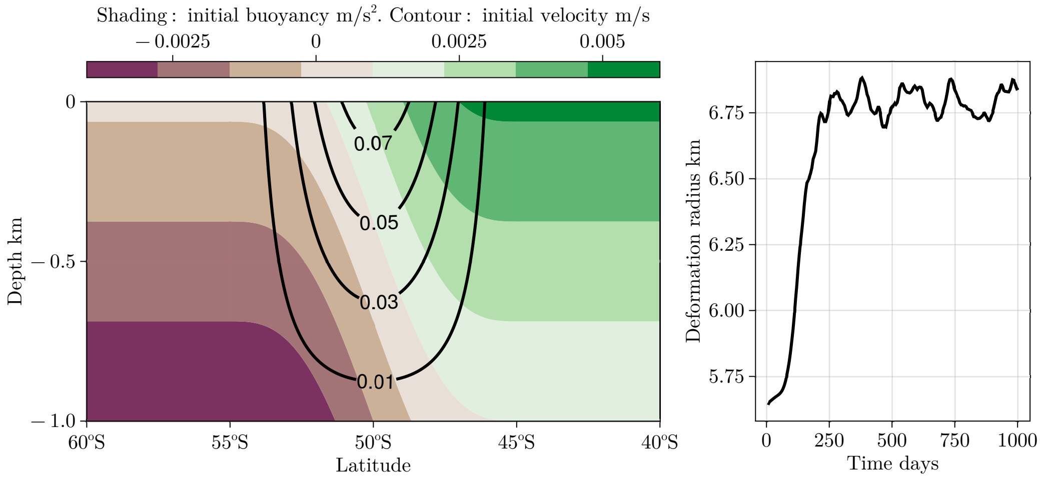

Figure 6. Left: The initial conditions (52): buoyancy (shading) and zonal velocity (contours). Right: The evolution of the domain-average deformation radius for the W9V case at 7km resolution.

commonly used in regional ocean modeling (Shchepetkin & McWilliams, 1998b; Madec et al., 2022).

Dispersive schemes are unstable without lateral diffusion, therefore, to benchmark against dispersive schemes, we consider a second-order energy-conserving discretization of the momentum advection term in the rotational form, stabilized by two different explicit closures: (1) a lateral friction closure composed by a laplacian and a bilaplacian combination of a static viscosity and a Smagorinsky-type eddy viscosity (SM2) described in Appendix A (Smagorinsky, 1963); (2) a quasi-geostrophic counterpart to the two-dimensional Leith closure, with $\mathbb{C} = 2$ (QG2), designed to satisfy the forward cascade of potential vorticity (Bachman et al., 2017). The details of these explicit closures are summarized in Appendix A. These explicit closures are not chosen because we believe that they are best in class, but rather because most OGMs use either a Smagorinsky closure, a Leith closure, a constant viscosity, or a combination of the three. Additional information about the test cases is given in tables 2 and 3.

Tracer advection is more expensive than rotational-form momentum advection given the three-dimensional nature of the scheme when compared to the two-dimensional vorticity flux. We find that a 7th-order tracer advection scheme is a good compromise between efficiency and accuracy, and for this reason, we use a 7th-order WENO scheme for buoyancy advection in all test cases. Each set consists of three simulations run with horizontal resolutions of 1/8th, 1/16th, and 1/32nd of a degree, equivalent to a maximum (meridional) grid spacing of 14 km, 7 km, and 3.5 km, respectively. The vertical grid spacing is fixed at 20 meters. The equations are evolved in time using a second-order Adams-Bashforth scheme and a subcycling scheme for the two-dimensional free surface.

The jet undergoes an initial baroclinic instability that develops into a statistically steady state around the 250th day, when the eddy kinetic energy dissipation balances the injection of potential energy generated by the buoyancy restoring. The most unstable mode of a baroclinically unstable jet is close to the deformation radius defined as (Vallis, 2017):

$$L_d \stackrel{\text{def}}{=} \frac{1}{\pi|f|} \int_{-H}^{0} (\partial_z b)^{1/2} \, \mathrm{d}z \; . \tag{54}$$

A fully resolved simulation requires a horizontal spacing finer than L_d. How much finer depends on the numerical scheme: given the vigorous inverse energy cascade characteristic of quasi-geostrophic turbulence, a lower dissipation results in convergence at a coarser resolution. An eddy-permitting simulation has a grid size of the same order as the deformation radius

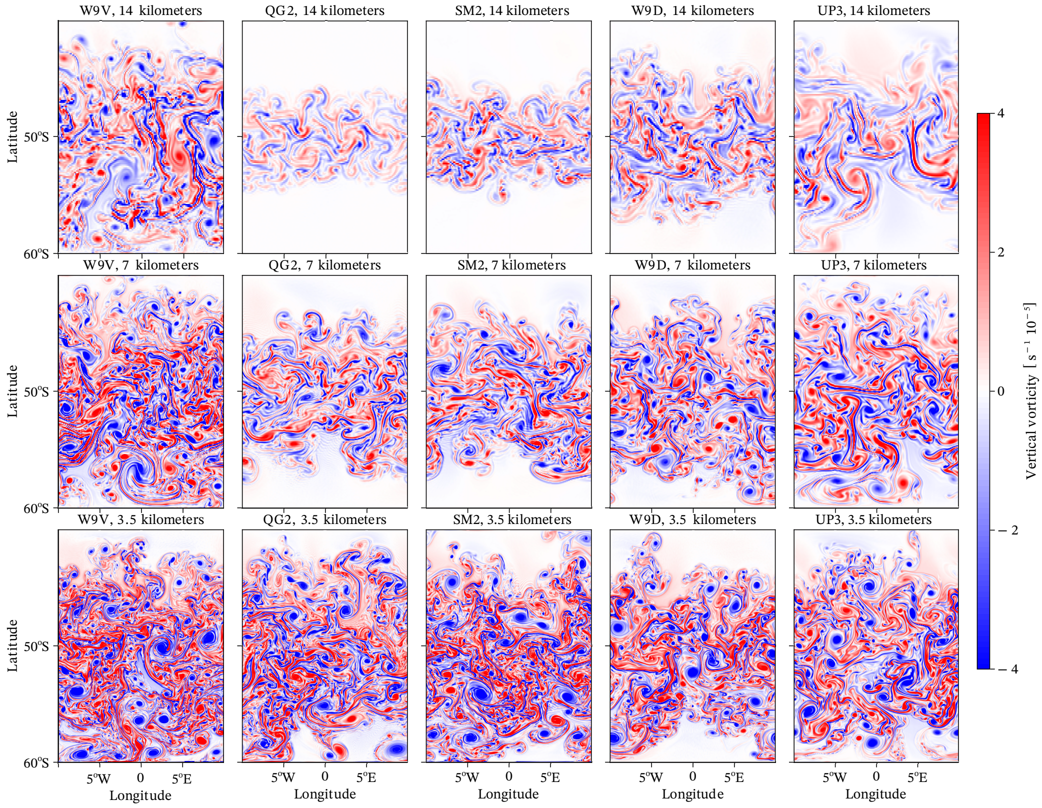

Figure 7. Near-surface vorticity at 14 (top panels), 7 (center panels), and 3.5-kilometer (bottom panels) resolution during the initial instability phase (day 230). The leftmost panel shows W9V while the remaining panels (from left to right) are ordered by increasing kinetic energy.

(10-50 km in the ocean). In this baroclinic jet setup, the initial deformation radius is 5.5 km and adjusts to an equilibrium value of about 6.75 km as shown in figure 6. Thus, the highest resolution simulations are barely "resolved" with slightly more than one grid cell per deformation radius, while the 14 km tests are "under-resolved". The 7-kilometer simulations are in a dynamical regime representative of typical eddy-permitting ocean models, which are run with a horizontal spacing between 10-20 km.

Figure 7 shows surface vorticity at different resolutions at the end of the initial transient (day 220). The panels are organized by increasing resolution from top to bottom and increasing kinetic energy from left to right (except the leftmost panels which show the W9V solution). As resolution increases, eddy activity spreads to higher and lower latitudes, indicating that the frontal slumping has extended further in the domain. Interestingly, W9V shows a large spread of vorticity even in the 14 km case where the deformation radius is severely under-resolved. The dispersive cases show evidence of spectral ringing at 7 and 3.5 km resolutions.

The time series of total kinetic energy, eddy kinetic energy, and eddy potential energy are shown in Figure 8. In the top panels, W9V is compared to the dispersive approaches (SM2, and QG2), while in the bottom panels W9V is compared to the diffusive schemes (UP3 and W9D). As expected, increasing resolution results in more APE to EKE conversion. The length of the initial transient until the solution becomes fully turbulent decreases with increasing resolution until it converges at 7 km for W9V, and at 3.5 km for all the other cases. We attribute this difference to the fact that all explicit closures assume fully turbulent flow, whereas during the initial transient the growth of baroclinic instability is laminar. The amount of implicit dissipation with W9V, instead, is proportional to the smoothness of the

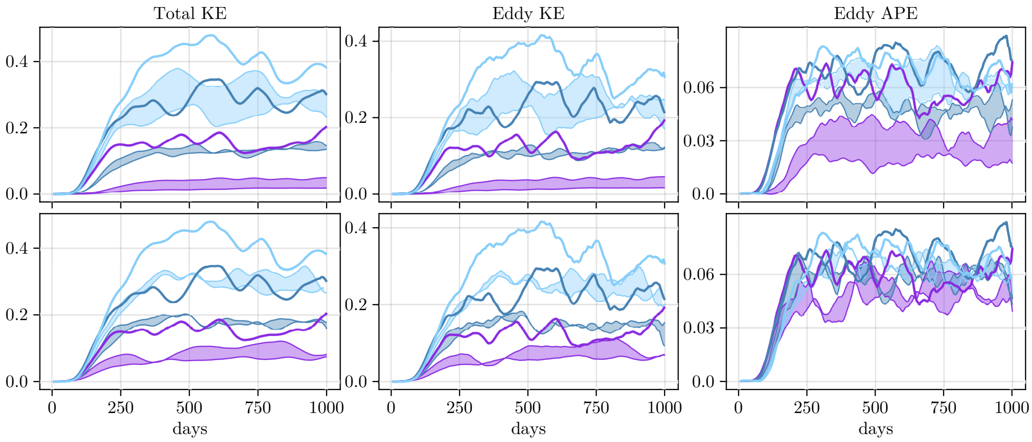

Figure 8. 10-day running average of integrated total kinetic energy, eddy kinetic energy, and eddy available potential energy. The solid lines are W9V at 14 km (blue), 7 km (steel blue), and 3.5 km resolution (light blue). The banded lines of the same colors show the maximum and minimum trajectory for the dispersive cases (top: SM2, QG2) and diffusive schemes (bottom: UP3, W9D).

resolved flow and thus smaller during the laminar phase as it should be. The panels in Figure 8 show that solutions using W9V converge at half the resolution (or more) during the initial instability growth.

The transformation of mean APE to EKE occurs through generation of eddy APE by baroclinic instability of the mean flow. The eddy APE is then converted to EKE through the vertical eddy flux ($w'b'$). Eddy available potential energy and eddy kinetic energy are further removed from the system by dissipation and by the restoring to thermal wind balance. The much larger EKE in the W9V cases when compared to the other test cases suggests that the implicit dissipation intrinsic in the W9V scheme is significantly lower than the (explicit) energy dissipation provided by the explicit closures and the (implicit) dissipation provided by the other diffusive schemes. This is substantiated by the near-surface spectra (averaged over days 250 to 1000) of energy, enstrophy, and vertical buoyancy flux, shown in figure 9. In particular, a larger dissipation when compared to W9V (1) damps the baroclinic instability as seen by the drop in $w'b'$ and (2) inhibits the transfer of energy to larger scales resulting in weaker large-scale flows (see the energy spectra in figure 9). Interestingly, despite the numerical similarity, there's a marked difference between W9V and W9D, demonstrating the critical importance of selecting an appropriate smoothness measure when employing WENO-based reconstruction within the rotational framework. While the kinetic energy plots exhibit significant differences between schemes and resolutions, the disparity isn't as pronounced in the eddy APE. However, in the lowest resolution dispersive cases, strong explicit energy dissipation inhibits the development of baroclinic instability by mitigating meridional velocity fluctuations. Consequently, there's a discernible effect on the eddy APE, which consistently remains lower compared to other solutions.

To judge the "effective" resolution of the different approaches we look at zonal mean buoyancy averaged between 250 and 1000 days. The final buoyancy slope is determined by a balance between the mean buoyancy restoring, forcing the system towards the initial low-stratification jet state, and mesoscale eddies which tend to restratify the system. We expect a larger stratification for cases that can maintain higher levels of eddy kinetic energy as the equilibrium is pushed toward a lower APE state. Figure 10 shows mean buoyancy contours for the different cases compared to W9V, where the filled contours show QG2 (top left), SM2 (top right), W9D (bottom left), and UP3 (bottom right) at 3.5-kilometer resolution, respectively. Figure 10 shows that, indeed, an increase in resolution leads to a more strongly stratified buoyancy profile, with W9V having a larger stratification than

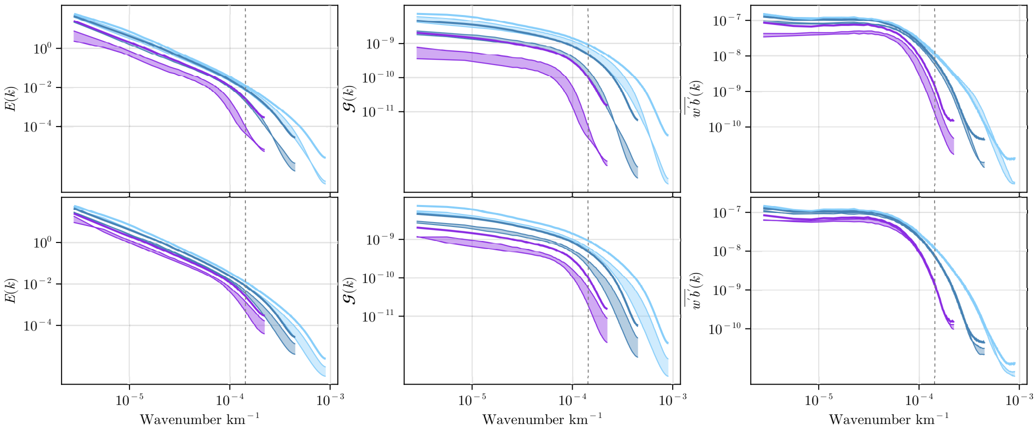

Figure 9. Time-averaged zonal energy spectra (left), enstrophy spectra (center), and $w'b'$ cospectra (right) averaged over the top 200 meters. The solid lines are W9V at 14 km (blue), 7 km (steel blue), and 3.5 km resolution (light blue). The banded lines of the same colors show the maximum and minimum trajectory for the dispersive cases (top: SM2, QG2) and diffusive schemes (bottom: UP3, W9D). The vertical dashed line shows the deformation radius.

all the other cases, in virtue of the larger EKE expressed by the model. Notably, the W9V buoyancy contours at 7-kilometer resolution are practically indistinguishable from the buoyancy contours of the other cases at 3.5-kilometer resolution, suggesting a similarly resolved mesoscale eddy field. Stratification for the W9V case at 3.5-kilometer resolution (not shown), is slightly larger than the other cases at 3.5-kilometer resolution indicating that convergence is still not achieved at 3.5 kilometers. However, convergence in this case is not expected, given that the deformation radius is only 6.75 kilometers. Achieving full conversion at this resolution would probably require a representation of the inverse energy cascade through a backscattering parameterization. This test case in a more complex mesoscale turbulence simulation confirms that the W9V method achieves a higher "effective" resolution compared to the other test cases.

6 Summary and Conclusions

We introduced a new momentum advection scheme for the rotational form of the primitive equation based on the WENO reconstruction of fluxed variables (vorticity, horizontal divergence, and kinetic energy gradient). We constructed the new momentum advection scheme as an alternative to using oscillatory advection schemes paired with explicit viscous closures, taking inspiration from "implicit" large eddy simulation. We achieved this by *(i)* rewriting the primitive equations to expose both vorticity and horizontal divergence, *(ii)* implementing a diffusive reconstruction of fluxed variables (vorticity, horizontal divergence, and kinetic energy gradient), and *(iii)* choosing smoothness indicators for the WENO scheme that reduce the energy dissipation inherent in the method.

We found that our proposed WENO scheme outperforms the Leith closure in decaying homogeneous two-dimensional turbulence across a broader range of resolutions. The scheme performed well also in an idealized "eddy-permitting" setting when compared to other approaches typically used in ocean modeling. Importantly, the scheme does not require any calibration of unknown coefficients, but rather it adjusts to varying resolutions attaining an intrinsic "scale-awareness".

By design the novel scheme significantly reduces dissipation, while efficiently removing variance at the grid-scale. We demonstrated that solutions obtained with our scheme are highly energetic and free from dispersive artifacts – a combination that has proven challenging

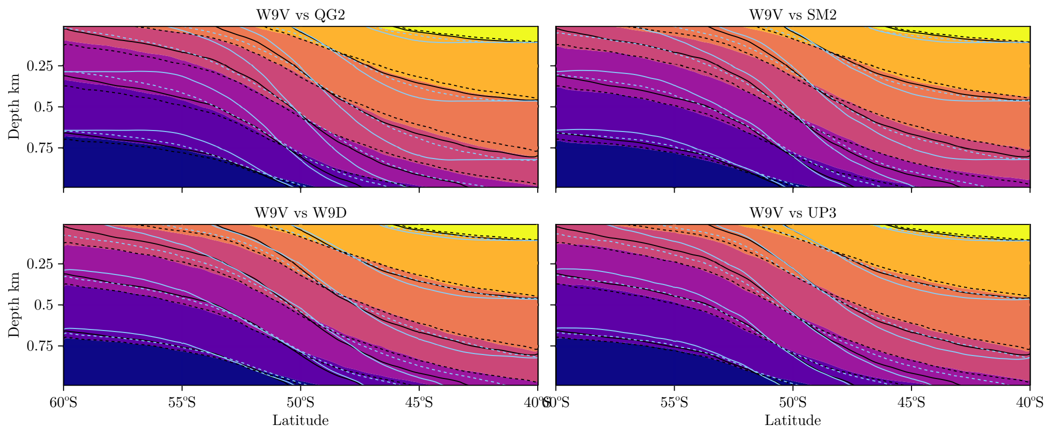

Figure 10. Left: Time and zonally averaged buoyancy for the different cases when compared to W9V. The filled contour shows the results of the comparative case (not W9V) at 3.5-kilometer resolution, acting as a reference, while the dashed and solid contours show solutions at 7 and 14-kilometer resolution, respectively. Black contours are the W9V case, while the light blue show the other case mentioned in the title of each frame (top left: QG2, top right: SM2, bottom left: W9D, bottom right: UP3).

to attain in "eddy-permitting" ocean flow regimes. In summary, our approach achieves a noise-free higher "effective" resolution when compared to the other dissipation approaches tested in this manuscript. The advantage of a higher "effective" resolution must be weighed against the additional cost of a numerical method involving high-order reconstruction stencils. In our GPU-based implementation, the W9V scheme in the idealized three-dimensional setting is only 20% more expensive than the most economical approach (UP3), while it has the same cost as the more complicated explicit closures (SM2 and QG2). It might be possible to obtain a similar time-to-solution with a lower order (7th for example) and a smaller grid-size as shown in Sanderson (1998).

We conclude by illustrating that the W9V advection scheme shows promise when implemented in an "eddy-permitting" near-global ocean model. The simulation is performed on a latitude-longitude grid with a horizontal resolution of 1/12-th of a degree spanning from 75°S to 75°N, 100 vertical levels, and realistic topography. The model is initialized from rest with temperature and salinity fields obtained from the data-constrained ECCO state estimate version 4 (Forget et al., 2015). The heat and salt fluxes are computed by restoring to the ECCO surface temperature and salinity fields. The surface wind stress is also taken from ECCO. The simulation is run for ten years with a time step of 270 seconds. The W9V method results in a stable and noise-free solution at the same computational cost of the QGLeith method, with the major advantage of requiring no tuning of parameters like a viscosity coefficient. Figure 1 shows the surface kinetic energy for the Gulf Stream and the Kuroshio current regions on March 1st, after 5 years of integration. The solution is characterized by vigorous turbulence that comprises of a web of frontal currents, without any signature of grid-scale noise. This near-global solution is only intended to showcase the feasibility of the proposed advection scheme in a realistic "eddy-permitting" ocean simulation. A detailed analysis of the accuracy of the solution is left for future work.

Appendix A Explicit closures used in this work

Two-dimensional Leith closure

The Leith closure is specifically designed for two-dimensional turbulence, where enstrophy undergoes a forward cascade and is removed at small scales by viscous dissipation. The explicit form of the effective viscosity is derived from spectral scaling arguments, where the scaling of the Kolmogorov wavenumber in two-dimensional isotropic homogeneous turbulence follows (Kraichnan, 1967). A series of assumptions on the shape of the spectral slope lead to an explicit eddy viscosity of the following form (Leith, 1996):

$$\nu_\star = \left(\frac{\mathbb{C}\Delta}{\pi}\right)^3 |\boldsymbol{\nabla}\zeta| \ , \tag{A1}$$

where $\mathbb{C}$ is a tunable parameter of order 1.

Quasi-Geostrophic (QG) Leith closure

Building upon the principles of the original Leith subgrid-scale model, the quasi-geostrophic (QG) Leith model (Bachman et al., 2017; Pearson et al., 2017), expands its applicability specifically to the simulation of geophysical flows. Unlike the original Leith model, the QG Leith model accounts for the peculiar characteristics of geophysical turbulence, where potential vorticity, instead of two-dimensional vorticity, undergoes a forward cascade. To account for this difference, Bachman et al. (2017) propose to substitute the gradient of vertical vorticity in equation (A1) with the gradient of potential vorticity. Where quasi-geostrophic dynamics do not hold (e.g. on the equator or in mixed layers), the closure reverts to the classical two-dimensional Leith formulation. The effective viscosity in the QG Leith formulation is expressed by

$$\nu_\star = \left(\frac{\mathbb{C}\Delta}{\pi}\right)^3 \left(\min\left(|\boldsymbol{\nabla} q_1|, |\boldsymbol{\nabla} q_2|, |\boldsymbol{\nabla} q_3|\right)^2 + |\boldsymbol{\nabla}(\boldsymbol{\nabla}\cdot\boldsymbol{u})|^2\right)^{1/2} \ , \tag{A2}$$

where

$$\boldsymbol{\nabla} q_1 = \boldsymbol{\nabla} q + \partial_z\left(\frac{f}{N^2}\boldsymbol{\nabla} b\right) \ , \quad \boldsymbol{\nabla} q_2 = \boldsymbol{\nabla} q\left(1 + \frac{1}{\mathrm{Bu}}\right) \ , \quad \boldsymbol{\nabla} q_3 = \boldsymbol{\nabla} q\left(1 + \frac{1}{\mathrm{Ro}^2}\right) \ , \tag{A3}$$

and $\boldsymbol{\nabla} q = \boldsymbol{\nabla}(\zeta + f)$. Bu and Ro above are the grid-scale Burger and Rossby numbers,

$$\mathrm{Bu} \overset{\text{def}}{=} \frac{\Delta^2}{L_d^2} \text{ and } \mathrm{Ro} \overset{\text{def}}{=} \frac{V}{|f|\Delta} \ , \tag{A4}$$

where V is a velocity scale (here assumed to be equal to 1)

Smagorinsky closure

The "Smagorinsky" based closure we used here is the OM4p25 lateral friction closure (Adcroft et al., 2019), a combination of a laplacian and a bilaplacian dissipation, with the viscosity calculated as a maximum between a static viscosity and a "Smagorinsky" type viscosity (Smagorinsky, 1963). Specifically,

$$\nu_{4,\star} = \max\left[\mathbb{C}_4\left(D_s^2 + D_t^2\right)^{0.5}\Delta^4, \ \mathbb{C}_4^u\Delta^3\right] \ , \tag{A5}$$

$$\nu_{2,\star} = \max\left[\mathbb{C}_2\left(D_s^2 + D_t^2\right)^{0.5}\Delta^2, \ \mathbb{C}_2^u\Delta\right]\mathbb{F} \, , \tag{A6}$$

where $\nu_{4,\star}$ and $\nu_{2,\star}$ are the bilaplacian and the laplacian viscosity, respectively, and

$$D_s = \partial_x u - \partial_y v \ , \quad D_t = \partial_x v + \partial_y u \, . \tag{A7}$$

Finally, $\mathbb{F} = \left(1 + 0.25\mathrm{Bu}^{-2}\right)^{-1}$ reduces the Laplacian viscosity where the deformation radius is resolved, and the value of the free parameters is

$$\mathbb{C}_4 = 0.06 \ , \quad \mathbb{C}_4^u = 0.01 \, , \quad \mathbb{C}_2 = 0.15 \ , \quad \mathbb{C}_2^u = 0.01 \, . \tag{A8}$$

Appendix B Divergence flux, conservative vertical advection form

We set out to demonstrate that in terms of discrete kinetic energy conservation, $\mathcal{V}$ is equivalent to $\mathcal{C}+\mathcal{D}$, or more specifically,

$$\sum_{i,j,k}\left(u\mathscr{V}_u\mathcal{V}_u + v\mathscr{V}_v\mathcal{V}_v\right) = \sum_{i,j,k}\left[u\mathscr{V}_u(\mathcal{C}_u+\mathcal{D}_u) + v\mathscr{V}_v(\mathcal{C}_v+\mathcal{D}_v)\right] . \tag{B1}$$

Note that the influence of boundary fluxes is not taken into account in the following derivation. Given two fields ϕ and ψ defined on a staggered C-grid, centered second-order reconstructions and differences satisfy these pointwise properties (Adcroft et al., 1997)

$$\langle\psi\rangle^i\langle\phi\rangle^i = \langle\psi\phi\rangle^i - \frac{1}{4}\delta_i\psi\,\delta_i\phi \,, \tag{B2}$$

$$\langle\delta_i\psi\rangle^i = \delta_i\langle\psi\rangle^i \,, \tag{B3}$$

$$\left\langle\langle\psi\rangle^i\phi\right\rangle^i = \psi\langle\phi\rangle^i + \frac{1}{4}\delta_i\left(\phi\delta_i\psi\right) \,, \tag{B4}$$

$$\delta_i\big(\langle\psi\rangle^i\phi\big) = \psi\delta_i\phi + \langle\phi\delta_i\psi\rangle^i \,, \tag{B5}$$

and these integral properties (Madec et al., 2022)

$$\sum_i\psi\langle\phi\rangle^i = \sum_i\langle\psi\rangle^i\phi \,, \tag{B6}$$

$$\sum_i\langle\psi\phi\rangle^i = \sum_i\psi\phi \,. \tag{B7}$$

Note that the volumes associated with variables ϕ and ψ (denoting the “location” of the two quantities) are implied and not explicitly indicated. Combining (B6) with (B7) and (B2), we can derive an additional integral property

$$\sum_i\psi\left\langle\langle\phi\rangle^i\right\rangle^i = \sum_i\psi\phi - \frac{1}{4}\sum_i\delta_i\psi\,\delta_i\phi \,. \tag{B8}$$

Focusing on the vertical advection term in the x-momentum equation ($\mathcal{V}_u$) and using property (B5):

$$\sum_{i,j,k}u\mathscr{V}_u\frac{\left\langle\langle W\rangle^i\delta_k u\right\rangle^k}{\mathscr{V}_u} = \underbrace{\sum_{i,j,k}u\mathscr{V}_u\frac{\left\langle\delta_k\left\langle\langle W\rangle^i\right\rangle^k u\right\rangle^k}{\mathscr{V}_u}}_{\text{term 1}} - \underbrace{\sum_{i,j,k}u\mathscr{V}_u\frac{\left\langle\left\langle u\delta_k\langle W\rangle^i\right\rangle^k\right\rangle^k}{\mathscr{V}_u}}_{\text{term 2}} . \tag{B9}$$

Applying property (B3) followed by (B4) to term 1:

$$\text{term 1} = \sum_{i,j,k}u\mathscr{V}_u\underbrace{\frac{\delta_k\left(\langle W\rangle^i\langle u\rangle^k\right)}{\mathscr{V}_u}}_{\mathcal{C}_u} - \frac{1}{4}\sum_{i,j,k}u\delta_k\left(\delta_k\left(u\langle D\rangle^i\right)\right) . \tag{B10}$$

where we made use of the discrete incompressibility condition ($D=-\delta_k W$). Applying the same incompressibility condition to term 2 followed by (B3) and (B8) yields

$$\text{term 2} = \sum_{i,j,k}u\mathscr{V}_u\underbrace{\frac{u\langle D\rangle^i}{\mathscr{V}_u}}_{\mathcal{D}_u} - \frac{1}{4}\sum_{i,j,k}(\delta_k u)\,\delta_k\left(u\langle D\rangle^i\right) . \tag{B11}$$

Combining the two terms:

$$\sum_{i,j,k}u\mathscr{V}_u\mathcal{V}_u = \sum_{i,j,k}u\mathscr{V}_u(\mathcal{C}_u+\mathcal{D}_u) \tag{B12}$$

$$- \frac{1}{4}\sum_{i,j,k}\left(u\,\delta_k(\delta_k\left(u\langle D\rangle^i\right)) + (\delta_k u)\,\delta_k\left(u\langle D\rangle^i\right)\right) . \tag{B13}$$

Focusing on the second term on the RHS, using property (B7) on the second element in the summation yields

$$\sum_{i,j,k} u\mathscr{V}_u \mathcal{V}_u = \sum_{i,j,k} u\mathscr{V}_u(\mathcal{C}_u + \mathcal{D}_u) \tag{B14}$$

$$- \frac{1}{4}\sum_{i,j,k} \left(u\,\delta_k\left(\delta_k\left(u\left\langle D\right\rangle^i\right)\right) + \left\langle(\delta_k u)\,\delta_k\left(u\left\langle D\right\rangle^i\right)\right\rangle^k \right) . \tag{B15}$$

The second term on the RHS can now be reduced using (B5), where $\psi = u$ and $\phi = \delta_k\left(u\left\langle D\right\rangle^i\right)$, leading to

$$\sum_{i,j,k} u\mathscr{V}_u \mathcal{V}_u = \sum_{i,j,k} u\mathscr{V}_u(\mathcal{C}_u + \mathcal{D}_u) - \frac{1}{4}\sum_{i,j,k} \delta_k \left(u\left\langle \delta_k\left(u\left\langle D\right\rangle^i\right)\right\rangle^k \right) , \tag{B16}$$

where the second term is the divergence of a vertical flux and, as such, its integral in the domain is equal to zero, leaving

$$\sum_{i,j,k} u\mathscr{V}_u \mathcal{V}_u = \sum_{i,j,k} u\mathscr{V}_u(\mathcal{C}_u + \mathcal{D}_u) . \tag{B17}$$

The same can be done for the v component leading to (B1).

Appendix C Upwinding of the discrete horizontal divergence

Contrary to vorticity reconstruction, straightforward upwinding of the horizontal divergence might not always lead to a decrease in discrete kinetic energy. To demonstrate this, we consider a first-order upwind reconstruction, for which

$$u\left\{c\right\}^i = u\left\langle c\right\rangle^i - \frac{|u|}{2}\delta_i c . \tag{C1}$$

With the above reconstruction scheme, the discrete divergence flux is

$$u\frac{\left\{D\right\}^i}{\mathscr{V}_u}\hat{\boldsymbol{\imath}} + v\frac{\left\{D\right\}^j}{\mathscr{V}_v}\hat{\boldsymbol{\jmath}} = \underbrace{\mathcal{D}_i\hat{\boldsymbol{\imath}} + \mathcal{D}_j\hat{\boldsymbol{\jmath}}}_{\substack{\text{energy}\\\text{conserving}}} - \underbrace{\left(|u|\frac{\delta_i D}{2\mathscr{V}_u}\hat{\boldsymbol{\imath}} + |v|\frac{\delta_j D}{2\mathscr{V}_v}\hat{\boldsymbol{\jmath}}\right)}_{\text{not energy conserving}} . \tag{C2}$$

The associated change in discrete integrated kinetic energy reads

$$\partial_t \sum_{i,j,k}(u^2\mathscr{V}_u + v^2\mathscr{V}_v + w^2\mathscr{V}_w) = \underbrace{\sum_{i,j,k}\left(u|u|\delta_i\delta_i U + v|v|\delta_j\delta_j V\right)}_{\text{negative definite}} + \sum_{i,j,k}\left(u|u|\delta_i\delta_j V + v|v|\delta_j\delta_i U\right) , \tag{C3}$$

where D has been divided into its two components ($\delta_i U$ and $\delta_j V$). Using (B5), we can show that the first term on the RHS is negative definite:

$$u|u|\delta_i\delta_i U = \delta_i\left(\left\langle u|u|\right\rangle^i \delta_i U\right) - \left\langle |u|\delta_i U\delta_i u\right\rangle^i - \left\langle u\delta_i U\delta_i |u|\right\rangle^i , \tag{C4}$$

where the first term is the divergence of a flux and, provided that the discrete areas do not change drastically in neighboring cells,

$$u\delta_i U\delta_i|u| = |u|\delta_i U\delta_i u \geq 0 . \tag{C5}$$

The same can be shown for $v|v|\delta_j\delta_j V$. Assuming that horizontally divergent motions are small

$$\delta_i U \sim -\delta_j V , \tag{C6}$$

the second term on the RHS of (C3) is

$$\sum_{i,j,k} \left(u|u|\delta_i \delta_j V + v|v|\delta_j \delta_i U \right) \sim - \sum_{i,j,k} \left(u|u|\delta_i \delta_i U + v|v|\delta_j \delta_j V \right) \ , \tag{C7}$$

which is positive definite and counteracts the energy dissipation provided by the first term on the RHS of (C3). As such, upwinding the discrete divergence might have the undesired effect of injecting energy at the grid scale instead of removing it. To avoid adding kinetic energy at the grid scale, we apply a diffusive reconstruction only to the terms that lead to discrete energy dissipation (where the reconstruction direction is the same as the difference direction) while maintaining a centered reconstruction for the terms that could lead to energy production (where reconstruction and difference directions are perpendicular).

Open Research Section

The momentum advection scheme described in this paper is implemented in Oceananigans.jl (Ramadhan et al., 2020) starting from version 0.84.0 (`https://github.com/CliMA/Oceananigans.jl/releases/tag/v0.84.0`). Visualizations were made using Makie.jl (Danisch & Krumbiegel, 2021). Scripts for reproducing and visualizing the idealized baroclinic setups are available at Silvestri (2024).

Acknowledgments

Our work is supported by the generosity of Eric and Wendy Schmidt by recommendation of the Schmidt Futures program and by the National Science Foundation grant AGS-1835576. N.C.C. is supported by the Australian Research Council DECRA Fellowship DE210100749. We would also like to acknowledge the three anonymous reviewers and the handling editor for their constructive input that greatly improved the manuscript.

References

Adcroft, A., Anderson, W., Balaji, V., Blanton, C., Bushuk, M., Dufour, C., ... Zhang, R. (2019). The GFDL global ocean and sea ice model OM4.0: Model description and simulation features. *Journal of Advances in Modeling Earth Systems*, *11*(10), 3167-3211. doi: 10.1029/2019MS001726

Adcroft, A., Hill, C., & Marshall, J. (1997). Representation of topography by shaved cells in a height coordinate ocean model. *Monthly Weather Review*, *125*(9), 2293-2315. doi: 10.1175/1520-0493(1997)125<2293:ROTBSC>2.0.CO;2

Arakawa, A. (1966). Computational design for long-term numerical integration of the equations of fluid motion: Two-dimensional incompressible flow. Part I. *Journal of Computational Physics*, *1*(1), 119-143. doi: 10.1016/0021-9991(66)90015-5

Arakawa, A., & Lamb, V. (1977). Computational design of the basic dynamical processes of the UCLA general circulation model. In J. Chang (Ed.), *General circulation models of the atmosphere* (Vol. 17, p. 173-265). Elsevier. doi: 10.1016/B978-0-12-460817-7.50009-4

Bachman, S., Fox-Kemper, B., & Pearson, B. (2017). A scale-aware subgrid model for quasi-geostrophic turbulence. *Journal of Geophysical Research: Oceans*. doi: 10.1002/2016JC012265

Balsara, D., & Shu, C. (2000). Monotonicity preserving weighted essentially non-oscillatory schemes with increasingly high order of accuracy. *Journal of Computational Physics*, *160*(2), 405-452. doi: 10.1006/jcph.2000.6443

Bates, J. R., & McDonald, A. (1982). Multiply-upstream, semi-Lagrangian advective schemes: Analysis and application to a multi-level primitive equation model. *Monthly Weather Review*, *110*(12), 1831-1842. doi: 10.1175/1520-0493(1982)110<1831:MUSLAS>2.0.CO;2

Danisch, S., & Krumbiegel, J. (2021). Makie.jl: Flexible high-performance data visualization for Julia [software]. *Journal of Open Source Software*, *6*(65), 3349. doi: 10.21105/joss.03349

Ding, M., Liu, H., Lin, P., Meng, Y., Zheng, W., An, B., ... Chen, K. (2022). A century-long eddy-resolving simulation of global oceanic large- and mesoscale state. *Scientific Data*, *9*(1), 691. doi: 10.1038/s41597-022-01766-9

Fenty, I., & Wang, O. (2020). *ECCO geometry parameters for the Lat-Lon-Cap 90 (llc90) native model grid (version 4 release 4).* NASA Physical Oceanography Distributed Active Archive Center. doi: 10.5067/ECL5A-GRD44

Forget, G., Campin, J.-M., Heimbach, P., Hill, C., Ponte, R., & Wunsch, C. (2015). ECCO version 4: an integrated framework for non-linear inverse modeling and global ocean state estimation. *Geoscientific Model Development*, *8*(10), 3071–3104. doi: 10.5194/gmd-8-3071-2015

Fox-Kemper, B., & Menemenlis, D. (2004). Can large eddy simulation techniques improve mesoscale rich ocean models? In M. Hecht & H. Hasumi (Eds.), *Ocean modeling in an eddying regime* (pp. 319 – 337). doi: 10.1029/177GM19

Gent, P., & Mcwilliams, J. (1990). Isopycnal mixing in ocean circulation models. *Journal of Physical Oceanography*, *20*(1), 150-155. doi: 10.1175/1520-0485(1990)020<0150:IMIOCM>2.0.CO;2

Hahn, S., & Iaccarino, G. (2008). Simulations of vortex-dominated flows: adaptive vorticity confinement vs. rotational-form upwinding. *Center for Turbulence Research, Annual Research Brief*.

Harten, A., Engquist, B., Osher, S., & Chakravarthy, S. (1987). Uniformly high order accurate essentially non-oscillatory schemes, III. *Journal of Computational Physics*, *71*(2), 231-303. doi: 10.1016/0021-9991(87)90031-3

Holland, W., Chow, J., & Bryan, F. (1998). Application of a third-order upwind scheme in the NCAR ocean model. *Journal of Climate*, *11*(6), 1487-1493. doi: 10.1175/1520-0442(1998)011<1487:AOATOU>2.0.CO;2

Ishiko, K., Ohnishi, N., Ueno, K., & Sawada, K. (2009). Implicit large eddy simulation of two-dimensional homogeneous turbulence using weighted compact nonlinear scheme. *Journal of Fluids Engineering*. doi: 10.1115/1.3077141

Karaca, M., Lardjane, N., & Fedioun, I. (2012). Implicit large eddy simulation of high-speed non-reacting and reacting air/H2 jets with a 5th order WENO scheme. *Computers & Fluids*, *62*, 25-44. doi: 10.1016/j.compfluid.2012.03.013

Kraichnan, R. (1967). Inertial ranges in two-dimensional turbulence. *The Physics of Fluids*, *10*(7), 1417-1423. doi: 10.1063/1.1762301

Leith, C. (1996). Stochastic models of chaotic systems. *Physica D: Nonlinear Phenomena*, *98*(2), 481-491. (Nonlinear Phenomena in Ocean Dynamics) doi: 10.1016/0167-2789(96)00107-8

Li, Y., Liu, H., Ding, M., Lin, P., Yu, Z., Yu, Y., ... Wang, P. (2020). Eddy-resolving simulation of cas-licom3 for phase 2 of the ocean model intercomparison. *Project. Adv. Atmos. Sci.*, *37*, 1067 – 1080. doi: 10.1007/s00376-020-0057-z

Madec, G., Bourdallé-Badie, R., Chanut, J., Clementi, E., Coward, A., Ethé, C., ... Moulin, A. (2022, March). *NEMO ocean engine.* Zenodo. doi: 10.5281/zenodo.6334656

Madec, G., & Imbard, M. (1996). A global ocean mesh to overcome the North pole singularity. *Climate Dynamics*, *12*, 381-388. doi: 10.1007/BF00211684

Maulik, R., & San, O. (2018). Explicit and implicit LES closures for Burgers turbulence. *Journal of Computational and Applied Mathematics*, *327*, 12-40. doi: 10.1016/j.cam.2017.06.003

Mohammadi-Aragh, M., Klingbeil, K., Brüggemann, N., Eden, C., & Burchard, H. (2015). The impact of advection schemes on lateral shear and baroclinic instabilities. *Ocean Modelling*, *94*, 112–127. doi: 10.1016/j.ocemod.2015.07.021

Norman, M. R., Eldred, C., & Meena, M. G. (2023). Investigating inherent numerical stabilization for the moist, compressible, non-hydrostatic euler equations on collocated grids. *Journal of Advances in Modeling Earth Systems*, *15*(10), e2023MS003732. doi:

10.1029/2023MS003732

Osher, S., & Shu, C. (1991). High-order essentially nonoscillatory schemes for Hamilton–Jacobi equations. *SIAM Journal on Numerical Analysis*, *28*(4), 907-922. doi: 10.1137/0728049

Pearson, B., Fox-Kemper, B., Bachman, S., & Bryan, F. (2017). Evaluation of scale-aware subgrid mesoscale eddy models in a global eddy-rich model. *Ocean Modelling*, *115*, 42-58. doi: 10.1016/j.ocemod.2017.05.007

Pressel, K., Mishra, S., Schneider, T., Kaul, M., & Tan, Z. (2017). Numerics and subgrid-scale modeling in large eddy simulations of stratocumulus clouds. *Journal of Advances in Modeling Earth Systems*, *9*(2), 1342-1365. doi: 10.1002/2016MS000778

Ramadhan, A., Wagner, G. L., Hill, C., Campin, J.-M., Churavy, V., Besard, T., ... Ferrari, R. (2020). Oceananigans.jl: Fast and friendly geophysical fluid dynamics on GPUs [Software]. *The Journal of Open Source Software*, *4*(44), 1965. doi: 10.21105/joss.01965

Ringler, T. D. (2011). Momentum, vorticity and transport: Considerations in the design of a finite-volume dynamical core. In P. Lauritzen, C. Jablonowski, M. Taylor, & R. Nair (Eds.), *Numerical techniques for global atmospheric models* (pp. 143–183). Berlin, Heidelberg: Springer Berlin Heidelberg. doi: 10.1007/978-3-642-11640-7_7

Ronchi, C., Iacono, R., & Paolucci, P. (1996). The "cubed sphere": A new method for the solution of partial differential equations in spherical geometry. *Journal of Computational Physics*, *124*(1), 93-114. doi: 10.1006/jcph.1996.0047

Roullet, G., & Gaillard, T. (2022). A fast monotone discretization of the rotating shallow water equations. *Journal of Advances in Modeling Earth Systems*. doi: 10.1029/2021MS002663

Sanderson, B. (1998). Order and resolution for computational ocean dynamics. *Journal of Physical Oceanography*, *28*(6), 1271 - 1286. doi: 10.1175/1520-0485(1998)028<1271:OARFCO>2.0.CO;2

Schwarzkopf, F. U., Biastoch, A., Böning, C. W., Chanut, J., Durgadoo, J. V., Getzlaff, K., ... Schubert, R. (2019). The inalt family – a set of high-resolution nests for the agulhas current system within global nemo ocean/sea-ice configurations. *Geoscientific Model Development*, *12*(7), 3329–3355. doi: 10.5194/gmd-12-3329-2019

Shchepetkin, A., & McWilliams, J. (1998a). Quasi-monotone advection schemes based on explicit locally adaptive dissipation. *Monthly Weather Review*, *126*(6), 1541-1580. doi: 10.1175/1520-0493(1998)126<1541:QMASBO>2.0.CO;2

Shchepetkin, A., & McWilliams, J. C. (1998b). Quasi-monotone advection schemes based on explicit locally adaptive dissipation. *Monthly Weather Rev*, *126*, 1541-1580.

Shu, C. (1997). *Essentially non-oscillatory and weighted essentially non-oscillatory schemes for hyperbolic conservation laws* (ICASE Report No. 97-65). Institute for Computer Applications in Science and Engineering, NASA Langley Research Center.

Silvestri, S. (2024). BaroclinicAdjustment.jl: v0.1.0, [software]. *Zenodo*. doi: 10.5281/zenodo.10719976

Silvestri, S., Wagner, G. L., Hill, C. N., Ardakani, M. R., Blaschke, J., Campin, J.-M., ... Ferrari, R. (2023). Oceananigans.jl: A model that achieves breakthrough resolution, memory and energy efficiency in global ocean simulations. (arXiv:2309.06662) doi: 10.48550/arXiv.2309.06662

Smagorinsky, J. (1963). General circulation experiments with the primitive equations: I. the basic experiment. *Monthly Weather Review*, *91*(3), 99-164. doi: 10.1175/1520-0493(1963)091<0099:GCEWTP>2.3.CO;2

Smolarkiewicz, P., & Margolin, L. (1998). MPDATA: A finite-difference solver for geophysical flows. *Journal of Computational Physics*, *140*(2), 459-480. doi: 10.1006/jcph.1998.5901

Soufflet, Y., Marchesiello, P., Lemarié, F., Jouanno, J., Capet, X., Debreu, L., & Benshila, R. (2016). On effective resolution in ocean models. *Ocean Modelling*, *98*, 36-50. doi: 10.1016/j.ocemod.2015.12.004

Souza, A., He, J., Bischoff, T., Waruszewski, M., Novak, L., Barra, V., ... Schneider, T. (2023). The flux-differencing discontinuous galerkin method applied to an idealized fully compressible nonhydrostatic dry atmosphere. *Journal of Advances in Modeling*

Earth Systems, *15*(4), e2022MS003527. doi: 10.1029/2022MS003527

Su, Z., Wang, J., Klein, P., Thompson, A., & Menemenlis, D. (2018). Ocean submesoscales as a key component of the global heat budget. *Nature Communications*, *9*(1), 775. doi: 10.1038/s41467-018-02983-w

Sytine, I., Porter, D., Woodward, P., Hodson, S., & Winkler, K.-H. (2000). Convergence tests for the piecewise parabolic method and Navier–Stokes solutions for homogeneous compressible turbulence. *Journal of Computational Physics*, *158*(2), 225-238. doi: 10.1006/jcph.1999.6416

Vallis, G. K. (2017). *Atmospheric and oceanic fluid dynamics*. Cambridge University Press.

Van Leer, B. (1977). Towards the ultimate conservative difference scheme. IV. A new approach to numerical convection. *Journal of Computational Physics*, *23*(3), 276-299. doi: 10.1016/0021-9991(77)90095-X

Woodward, P., & Colella, P. (1984). The numerical simulation of two-dimensional fluid flow with strong shocks. *Journal of Computational Physics*, *54*(1), 115-173. doi: 10.1016/0021-9991(84)90142-6

Zalesak, S. (1979). Fully multidimensional flux-corrected transport algorithms for fluids. *Journal of Computational Physics*, *31*(3), 335-362. doi: 10.1016/0021-9991(79)90051-2

Zeng, K., Li, Z., Rana, Z., & Jenkins, K. (2021). Implicit large eddy simulations of turbulent flow around a square cylinder at Re=22,000. *Computers & Fluids*, *226*, 105000. doi: 10.1016/j.compfluid.2021.105000